THESIS FOR THE DEGREE OF LICENTIATE OF ENGINEERING

COUPLING DYNAMICS OF LIGHT IN MULTI-CORE OPTICAL FIBERS

Manish Raj

Photonics Laboratory
Department of Microtechnology and Nanoscience - MC2
Chalmers University of Technology
Göteborg, Sweden, 2026

Coupling Dynamics of Light in Multi-Core Optical Fibers
Manish Raj

Chalmers University of Technology
Microtechnology and Nanoscience - MC2
Photonics Laboratory
SE-412 96 Göteborg, Sweden
Telephone: +46 (0) 76 454 5763

ISSN 1652-0769
Technical Report MC2-482

Front cover illustration: A coupled dual-core fiber with one excited core, illustrating propagation through symmetric and antisymmetric supermodes and nonlinear suppression of inter-core crosstalk in the high-power regime. Credits: Vijay Shekhawat (visual refinement).

Printed in Sweden by
Reproservice
Chalmers University of Technology
Göteborg, Sweden, July 2026

Coupling Dynamics of Light in Multi-Core Optical Fibers
Manish Raj
Photonics Laboratory
Department of Microtechnology and Nanoscience - MC2
Chalmers University of Technology, Göteborg, Sweden

Abstract

Space-division multiplexing (SDM) has emerged as one of the most promising technologies to meet the ever-increasing demand for data transmission driven by the rapid growth of modern data centers and artificial intelligence. The coupling characteristics of SDM devices, such as coupled-core multi-core fibers, determine the exchange of optical power among spatial and polarization modes, which significantly influence the system performance. Characterizing the coupling dynamics in the frequency and time domains provides fundamental insight into the underlying dynamics of SDM systems. This thesis focuses on the linear and non-linear characterization of coupling dynamics in coupled-core multi-core fibers. The linear coupling characteristics such as frequency and temporal dependence, directly affect the transfer function governing the propagation of spatial and polarization modes in coupled-core multi-core fibers, whereas nonlinear phenomena, such as wavelength conversion and inter-core crosstalk suppression, play a crucial role in the performance and functionality of SDM systems. In addition, a statistical model has been developed to describe the temporal dynamics of random mode coupling, providing insight into the stochastic evolution and temporal stability of the coupled-core multi-core fiber channels.

Keywords: Space-division multiplexing, Coupled-core multi-core fibers, Random mode coupling, Spatial modes, Polarization modes, Dirichlet distribution, Parametric interactions, Four-wave mixing.

Publications

This thesis is based on the work contained in the following papers:

[A] M. Raj, V. Ribeiro, G. Bouwmans, Y. Quiquempois, A. Mussot, P. Andrekson, M. Karlsson, "Investigation of Nonlinear Coupling and Parametric Interactions in Coupled Multi-Core Fibers", *European Conference on Optical Communications (ECOC)*, pp. 1–4, IEEE, 2025.

[B] M. Raj, T. Hayashi, P. Andrekson, M. Karlsson, "Statistical analysis of the temporal dynamics of coupling in strongly coupled multicore fibers", *Optics Express*, **34**, 25321–25333, 2026.

[C] M. Raj, L. A. Zischler, G. Di Sciullo, T. Hayashi, A. Mecozzi, C. Antonelli, M. Karlsson, "Statistical Characterization of Spatial and Polarization Mode Coupling in Field-Deployed Coupled-Core Multi-Core Fibers", *European Conference on Optical Communications (ECOC)*, 2026, accepted for publication.

[D] L. A. Zischler, C. Lasagni, M. Raj, G. Di Sciullo, M. Karlsson, P. Serena, A. Bononi, T. Hayashi, A. Mecozzi, C. Antonelli, "Experimental Observation of Modal-Dispersion-Induced FWM Efficiency Increase and Non-linearity Coefficient Characterization in Deployed Coupled-Core Multi-Core Fibers", *European Conference on Optical Communications (ECOC)*, 2026, accepted for publication.

Contents

Abstract iii

Publications v

Acknowledgment ix

Acronyms xi

1 Introduction 1
- 1.1 Motivation . . . 1
- 1.2 Historical Background . . . 1
- 1.3 This thesis . . . 5
  - 1.3.1 Thesis outline . . . 6

2 Fundamentals of Multi-Core Fibers 7
- 2.1 Multi-Core Fiber Classification . . . 7
- 2.2 Limitations of MCF Technology . . . 9
- 2.3 Mode Coupling in Multi-Core Fibers . . . 10
  - 2.3.1 Ideal Mode Coupling . . . 12
  - 2.3.2 Random Mode Coupling . . . 17
- 2.4 Impairments in MCF Systems . . . 20
  - 2.4.1 Inter-core Crosstalk . . . 20
  - 2.4.2 Group Delay Spread . . . 21
  - 2.4.3 Mode-dependent Loss . . . 22

3 Nonlinear Interactions in Coupled MCFs 25
- 3.1 Stimulated Brillouin Scattering . . . 25
- 3.2 Four-Wave Mixing . . . 30
  - 3.2.1 Phase Matching Condition . . . 31
  - 3.2.2 Wavelength Conversion in Multi-Core Fibers . . . 33

3.2.3 Experimental Implementation 35
3.3 Power-Dependent Mode Coupling 36
3.4 Modal Dispersion-Induced FWM 40
3.4.1 Experimental Implementation 42
3.4.2 Enhanced FWM by Modal Dispersion 43

4 Statistical Model for Random Mode Coupling 45
4.1 Temporal Dynamics of Random Coupling 45
4.1.1 Spatial and Polarization Mode Coupling 46
4.1.2 Experimental Implementation 48
4.2 Time-varying Random Coupling Model 51
4.3 Probability and Correlation Functions 53
4.3.1 Symmetric Dirichlet Distribution 53
4.3.2 Autocorrelation function 58

5 Summary and Future Outlook 61

6 Summary of Papers 65

Included papers A–D 83

Acknowledgment

First, I express my deepest gratitude to my supervisor, Prof. Magnus Karlsson, for giving me the opportunity to pursue the PhD and for his continuous support, guidance, and encouragement throughout the journey. His insight, patience, and trust have been invaluable to my growth as a researcher. I am also grateful to my co-supervisor, Prof. Peter Andrekson, for his motivation, thoughtful advice, and constructive feedback, which encouraged me to always do my best. I would also like to acknowledge Prof. Victor Torres Company for his inspiring approach to research and teaching, from which I learned a lot as a teaching assistant.

My sincere thanks go to Prof. Cristian Antonelli for welcoming me to the INCIPICT Lab at the University of L'Aquila, Italy, and for his mentorship during my secondment. I also thank Dr. Giammarco Di Sciullo, Divya Ann Shaji and Lucas Alves Zischler for their generous assistance and for making my stay in L'Aquila both productive and memorable. In addition, I would like to acknowledge Dr. Vitor Ribeiro for his significant contribution to the simulation studies of nonlinear effects in dual-core fiber and for sharing his expertise throughout this work.

A special thanks goes to Dr. Ekaterina Deriushkina for her guidance and support at the beginning of my start in the Photonics Laboratory. She introduced me to the lab environment and made my transition to research smoother. I am also grateful to Dr. Rasmus Larsson, Dr. Ruwan Udayanga, and Dr. Krishna Twayana for sharing their experience and for their helpful feedback and support. I also thank Vijay Shekhawat for his encouragement, thoughtful input, and many valuable discussions. Furthermore, I would like to thank everyone at the Photonics Laboratory for their kindness, support, and willingness to share ideas. Their encouragement and valuable discussions have greatly enriched my research, broadened my knowledge, and provided many useful insights along the way.

I also acknowledge the Horizon Europe HOMTech project and the Swedish Research Council for funding my research and providing me with the opportunity to interact with researchers and scholars within the Innovative Training Network (ITN), expand my professional network, and participate in PhD training schools. These experiences have contributed significantly to my academic and professional development.

My heartfelt thanks go to my family for their unconditional love, encouragement, and constant support. I am especially grateful to my wife for her patience, understanding and unwavering support throughout this journey. Finally, I would like to thank all my friends and family members for their encouragement, support and good wishes. This thesis would not have been possible without their support.

Manish Raj[1]
Göteborg, July 2026

[1]This thesis was written by the author. Large language models were used solely for language editing and stylistic refinement. All scientific content, analyses, results, interpretations, and conclusions are the author's own.

Acronyms

ASE	amplified spontaneous emission
CCF	coupled-core fiber
CMT	coupled-mode theory
CW	continuous wave
DGD	differential group delay
DSP	digital signal processing
DWDM	dense wavelength-division multiplexing
EDFA	erbium-doped fiber amplifier
FIFO	fan-in/fan-out
FMF	few-mode fiber
FWHM	full width at half maximum
FWM	four-wave mixing
GD	group delay
GDS	group delay spread
HNLF	highly nonlinear fiber
LLM	large language model
MCF	multicore fiber
MCVD	modified chemical vapor deposition
MDL	mode-dependent loss
MIMO	multiple-input multiple-output
NLSE	nonlinear Schrödinger equation
OSA	optical spectrum analyzer
OTDR	optical time-domain reflectometry
PBS	polarization beam splitter
PDF	probability density function
PM	phase modulator
PMD	polarization-mode dispersion
QAM	quadrature amplitude modulation
QPSK	quadrature phase-shift keying

RF	radio frequency
SBS	stimulated Brillouin scattering
SDM	space-division multiplexing
SMD	spatial-mode dispersion
SMF	single-mode fiber
SNR	signal-to-noise ratio
SOP	state of polarization
SPM	self-phase modulation
SSFM	split-step Fourier method
WDM	wavelength-division multiplexing
XPM	cross-phase modulation
ZDW	zero-dispersion wavelength

Chapter 1

Introduction

1.1 Motivation

We all enjoy streaming services such as Netflix, Amazon Prime Video, and various social media platforms [1]. The enormous volume of data generated by these services is transmitted through an invisible, hair-thin strand of optical fiber, which supports the transmission of petabytes of data per second. Information is commonly transmitted using electromagnetic waves propagating through physical media such as silica (ultra-pure glass) in the core and cladding, which have a small difference in refractive index. Light is guided through the core by the phenomenon of total internal reflection [2]. These optical fibers form the backbone of a modern digital system. With the surge in internet traffic and the huge data demands of large language models (LLMs), the single-mode fiber (SMF) infrastructure is being pushed to its limits [3]. In this chapter, we discuss the historical development of various tools and techniques introduced over the years for optical fiber communication systems.

1.2 Historical Background

In 1966, Charles Kao of Standard Telecommunication Laboratories in the UK predicted that high-purity, transition-metal-free glass fibers could achieve transmission losses below 20 dB/km [4]. For this pioneering work, he was awarded the Nobel Prize in Physics in 2009. Four years later, in 1970, Corning Glass Works in the US reported the first prototype silica glass optical fiber with a transmission loss below 20 dB/km [5]. This value became a landmark for optical fibers, achieving performance comparable to coaxial cables in terms of repeater spacing. Following this milestone, optical fiber development gained rapid momentum in the US, UK, and Japan.

In the early 1970s, Sumitomo Electric developed key optical fiber technologies, including vapor-phase axial deposition (VAD) [6] preform fabrication, tandem primary coating, and pure-silica cores [7]. In 1974, Bell Laboratories in the US achieved a transmission loss of 2 dB/km using the modified chemical vapor deposition (MCVD) method [8], which allowed precise control of the fiber composition and refractive index. This paved the way for high-performance optical fibers suitable for long-distance communication.

Over the years, improvements in low-loss transmission fibers have significantly increased the transmission distance and capacity of optical data transmission. Another major breakthrough came with the development of the erbium-doped fiber amplifier (EDFA) in 1987 by researchers at the University of Southampton [9]. The EDFA perfectly matches the low-loss window (C-band, roughly 1530–1565 nm) of standard silica optical fibers. It enabled optical signals to travel in submarine cables across trans-continental and trans-oceanic distances without the need to electronically detect and retransmit the signal. This has enabled fiber-optic systems to span the globe. Without EDFAs, long-distance optical communication would be limited and expensive.

The technology that further increased transmission capacity after the EDFA was wavelength-division multiplexing (WDM), which combines multiple wavelengths of light into a single optical fiber. Commercial WDM systems [10] became available as early as 1996. Together with EDFAs, which provide the gain bandwidth needed to amplify multiple wavelength channels simultaneously, this enabled far more efficient long-distance transmission. The technology later evolved into dense wavelength-division multiplexing (DWDM), with tightly spaced channels [11] (around 50 GHz spacing in the C-band), increasing network capacity by several hundred times.

The development of advanced modulation techniques [14] has significantly improved spectral efficiency and enabled much higher data transmission capacities. Coherent optical communication enabled the simultaneous detection of the amplitude and phase of optical signals [15], which allowed the use of higher-order modulation formats such as quadrature phase-shift keying (QPSK) and Quadrature Amplitude Modulation (QAM) [16,17]. It also enabled the use of digital signal processing (DSP)

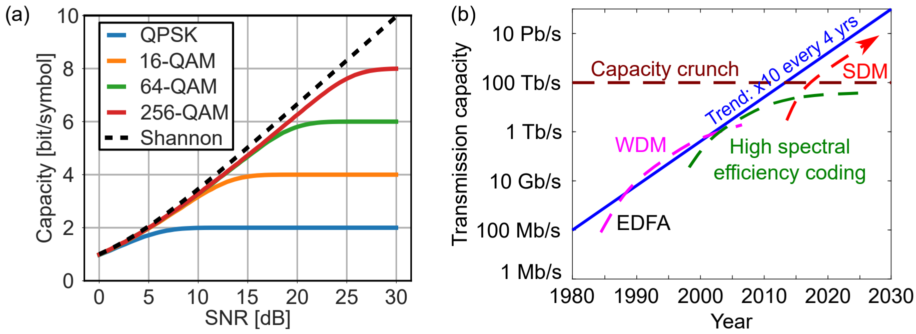

Figure 1.1: (a) Capacity limits of optical fiber networks [12] and (b) evolution of growing transmission capacity demand in optical fiber communication systems [13].

to electronically mitigate transmission impairments such as chromatic dispersion, phase delays, and polarization effects after signal detection. With this, it became possible to transmit many bits within the same bandwidth, providing extremely high spectral efficiency.

As spectral efficiency continued to improve, the transmission capacity of single-mode fiber approaches its practical upper bound, defined by the Shannon limit [12], as illustrated in Fig. 1.1(a). As input power increases, nonlinear effects dominate, and transmission capacity will not increase beyond a certain power [18]. One straightforward approach to increase transmission capacity is to deploy multiple single-mode fibers, for example SMFs packaged together in ribbon cables or fiber bundles, thereby increasing the number of parallel transmission channels, which is the conventional form of spatial-division multiplexing (SDM). However, this strategy does not fundamentally overcome the capacity limitation of a single optical fiber. According to the Shannon capacity relation [19], the achievable channel capacity increases logarithmically with the signal-to-noise ratio (SNR). Consequently, a substantial increase in capacity requires a disproportionately large increase in optical SNR and launched power, while fiber nonlinearities such as self-phase modulation and cross-phase modulation become increasingly significant at high powers. These limitations motivated the evolution of SDM towards a more integrated approach, where multiple spatial channels are supported within a single fiber cladding. Modern advanced SDM exploits the spatial dimension of an optical fiber [20] by transmitting independent data streams through multiple spatial channels in multi-core fibers (MCFs) or multiple guided modes in few-mode fibers (FMFs). By increasing the number of spatial channels within a common fiber structure, the overall transmission capacity can scale approximately linearly with the number of cores or modes, while reducing the cost, footprint and energy consumption per transmitted bit in long-haul communication systems. The evolution of optical communication systems is shown in Fig. 1.1(b).

The transmission capacity C [bit/s] of the SDM fibers scales linearly with the number of spatial channels and the transmitted power [19], as given by [21]

$$C = NB \log_2(1 + SNR), \tag{1.1}$$

where N represents the number of wavelength or spatial channels, B is the bandwidth per channel in Hertz, and SNR is the signal-to-noise ratio, defined as the ratio of the signal power to the noise power in the communication system.

SDM can be implemented using different fiber designs. One approach is multi-core fibers, where several cores are integrated within a single cladding to allow independent spatial data channels to propagate through each core. Another approach is few-mode fibers, which supports the transmission of multiple propagation modes within a single core. Although both techniques use different methods, their common objective is to overcome the capacity limit of conventional optical fibers and significantly enhance transmission capacity. Multi-core fibers were first proposed [22] in 1979, with single-mode weakly-coupled MCFs were introduced [23] in 1994. Over the past decade, MCFs have attracted significant research interest as a promising approach for increasing the transmission capacity per optical fiber. Petabit per second (Pb/s) data transmission have been demonstrated using wide-band wavelength division multiplexing in multi-core fibers, which marks a key advancement toward realization of ultra-high-throughput optical communication links [24, 25].

There are two main types of multi-core fibers: (a) uncoupled-core multi-core fibers and (b) coupled-core multi-core fibers [26]. In uncoupled-core multi-core fibers, the cores are sufficiently far apart to prevent significant power leakage between them, whereas in coupled-core multi-core fibers, the cores are placed close to one another, allowing light to couple from one core to adjacent cores. This power leakage is an major issue in these systems, as it causes inter-core crosstalk [27–29] that can affect signal integrity and ultimately limit system performance and transmission capacity. Characterizing inter-core crosstalk and coupled power is a crucial step to understand the dynamics of these fibers and fully exploit their capabilities for data transmission.

SDM-based transmission systems require an accurate channel model to optimize multiple-input multiple-output (MIMO) digital signal processing algorithms [30–32]. To understand the channel properties of multi-core-fibers, various characterization methods have been proposed to experimentally measure the transfer matrix [33–40]. Using the measured transfer matrix of a multi-core fiber, its channel model can be derived in the frequency and time domains. The transfer matrix of a coupled-core multi-core fiber system is also affected by inter-core coupling. Understanding the temporal and frequency dynamics of coupling is important for characterizing channel behavior [41]. In this thesis, we mainly focus on the linear and nonlinear characterization of coupling dynamics in coupled-core multi-core fibers.

1.3 This thesis

This thesis focuses on the coupling dynamics in coupled-core multi-core fibers. We have studied the statistical properties of the temporal dynamics of spatial and polarization mode coupling in the linear propagation regime. Furthermore, we experimentally investigated the nonlinear effects of coupling in these types of fibers. Studying parametric interactions, such as wavelength conversion, allows us to better understand the nonlinear properties of these fibers.

The papers included in this thesis complement each other. It describe the experimental techniques and demonstrate the results of coupling dynamics in coupled-core multi-core fibers. [Paper A] discusses the nonlinear effects in weakly-coupled multi-core fiber. The paper shows that the multi-core fiber is sensitive to longitudinally varying coupling coefficients, and at high power, most of the optical power remains in the same core. This leads to nonlinear suppression of the optical power transfer at high power. The paper also mentions the effect of coupling on wavelength conversion efficiency, where the phase-matching condition depends sensitively on the strength of coupling. [Paper B] is devoted to the characterization of the temporal dynamics of coupling in a strongly-coupled multi-core fiber. It shows that the statistical distribution of the fractional coupled power follows a beta distribution, which is a marginal distribution of the Dirichlet distribution. [Paper C] describes temporal drift of coupled power in a randomly-coupled multi-core fiber. It is shown that the fiber at short time is not isotropic and the distribution tends to be asymmetric, whereas with sufficiently long time, the isotropy is restored. The polarization modes are shown to decorrelate faster than the spatial modes, which explains the two different time scale of coupling dynamics in these types of fiber. [Paper D] is devoted to the experimental study of effect of modal dispersion on four-wave mixing (FWM) in a field-deployed randomly-coupled multi-core fiber. It shows that the FWM efficiency is enhanced by the presence of spatial mode dispersion (SMD). The nonlinear coefficient is also measured experimentally, showing a four-fold reduction in the effective nonlinearity of the randomly-coupled multi-core fiber compared with the co-deployed standard single-mode fiber.

1.3.1 Thesis outline

This thesis is organized as follows: Chapter 1 discusses the introduction and presents the historical background of the field. Chapter 2 covers the fundamentals of multi-core fibers and classifies MCFs based on types of coupling. Following this, the coupling mechanisms and impairments in multi-core fibers are discussed. Chapter 3 focuses on nonlinear effects in coupled-core multi-core fibers. The theory of stimulated Brillouin scattering and four-wave mixing in coupled-core multi-core fibers is described in detail. Wavelength conversion and the effect of coupling on conversion efficiency are also discussed. In addition, the chapter examines the frequency, polarization, and power dependence of mode coupling. Finally, the effect of modal dispersion on four-wave mixing efficiency is presented. Chapter 4 introduces the statistical model and characterization methods for random mode coupling. The statistical properties of the temporal dynamics of mode coupling, including the probability distribution function and the autocorrelation function, are also described in detail. Chapter 5 presents a summary and future outlook. Chapter 6 briefly mentions the main results reported in the appended papers.

Chapter 2

Fundamentals of Multi-Core Fibers

Over the years, the transmission capacity of optical communication systems has increased dramatically [42], driven by technological advances such as WDM, coherent detection, and DSP. To sustain this continuous growth, a variety of technologies have been introduced as described in chapter 1. In this chapter, the fundamentals and types of multi-core fibers based on their coupling regimes are presented. This chapter also includes an overview of mode coupling in multi-core fibers, which may be either ideal or random depending on whether the fiber is unperturbed or perturbed. Although MCFs technology offers numerous advantages to increase transmission capacity, it is subject to several impairments that can limit system performance and capacity. These impairments and their impact on high-capacity transmission systems are briefly discussed.

2.1 Multi-Core Fiber Classification

With wavelength, polarization, time, and modulation formats largely exploited, the spatial dimension of optical fibers has emerged as the remaining degree of freedom to increase transmission capacity. This approach is referred to as space-division multiplexing [43]. Unlike standard single-mode fiber, which contains a single core embedded in a common cladding, SDM fibers can incorporate multiple cores within the same cladding, forming a multi-core fiber structure [44]. Depending on the core pitch, i.e., the distance between adjacent core centers, MCFs can operate in either the weakly-coupled or strongly-coupled regime [45] as illustrated in figure 2.1. In addition to multi-core fibers, few-mode multi-core fibers and multi-mode fibers also enable parallel spatial channels [46], but they are not the subject of discussion in this thesis. In these fibers, higher-order spatial modes act as independent channels for transmitting optical data.

Multi-core fibers are classified into weakly-coupled multi-core fibers (WC-MCFs) and strongly-coupled multi-core fibers based on the nature of coupling between the cores [47]. The strongly-coupled MCFs are further categorized as systematically coupled and randomly coupled multi-core fibers (RC-MCFs). In a weakly-coupled MCF, the core pitch is large so that the mode coupling (crosstalk) between the cores is weak, and each core behaves as an isolated core that can be used as an independent spatial channel. It is also compatible with existing single mode fiber transceivers. Whereas, in a strongly-coupled MCF, the core pitch is small, the mode coupling between the cores is strong and not negligible. Depending on the transmission reach, weakly-coupled MCFs may exhibit behavior similar to strongly-coupled fibers in long-haul transmission, as crosstalk accumulates linearly with the propagation distance [48].

Strongly-coupled MCFs are classified into systematically-coupled MCFs, where inter-core coupling is strongest, and randomly-coupled MCFs, in which the coupling characteristics lie between those of weakly-coupled and systematically-coupled fibers. Systematically-coupled MCFs act as a single coupled micro-structured waveguide, in which the guided eigenmodes are superpositions of the local modes of individual cores, and the modes of the entire structure are referred to as supermodes and will be discussed in more detail in Section 2.3. In randomly-coupled MCFs, neither supermodes nor individual core modes remain stable during propagation, and the optical fields evolve through continuous random mixing along the fiber length. Such fiber is modeled with concatenated waveplate model, where each section is independent with neighboring sections and randomly-coupled with each other. Thus, the accumulated DGD and MDL scale with the square root of the propagation distance. Since the modes are randomly-coupled with each other during transmission, optical properties such as propagation loss and chromatic dispersion are averaged over the cores. Consequently, signal recovery in randomly-coupled MCF relies on MIMO DSP, which jointly and simultaneously processes the received signals from all coupled modes or cores to reverse the channel mixing and compensate for transmission impairments. In practice, the complexity of the required MIMO equalization depends on

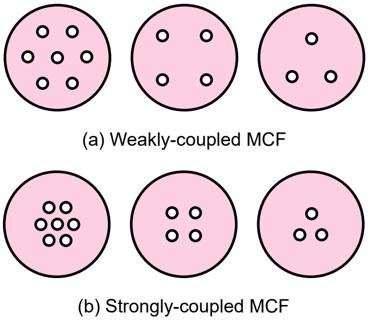

Figure 2.1: Multi-core fibers are classified according to their coupling regime into (a) weakly-coupled MCFs and (b) strongly-coupled MCFs.

the coupling regime. The classification of multi-core fibers is presented in Table 2.1.

2.2 Limitations of MCF Technology

Multi-core fiber offers greater transmission capacity in optical communication systems by allowing one or more spatial channels within a single fiber cladding, thereby significantly increasing the total data throughput. Another major benefit is easier scalability and improved efficiency. By delivering higher data throughput through the same fiber cable, it drastically reduces infrastructure costs, as fewer fiber cables are required to meet the requirements of network systems and data centers.

Despite the significant advantages of the multi-core fiber technology, there are still several manufacturing and technical challenges that must be addressed. These fibers are difficult to design and fabricate because they require precise control of core spacing and uniformity along the entire length of the fiber to minimize crosstalk and reduce modal dispersion effects. One of the major challenges in a multi-core fiber is inter-core crosstalk, where signals leak into adjacent cores and degrade the quality of the transmitted data. Understanding the nature of crosstalk in these fibers is essential for designing improved MCFs with better transmission performance [49]. Section 2.4 provides a detailed discussion of the key impairments in multi-core fibers. Another challenge is splicing of multi-core fibers. To properly splice multiple cores, very high precision is required in rotational alignment to ensure accurate core matching and to achieve low splice loss. Conventional single-mode fiber splicers are not sufficient for this purpose, so we require more advanced splicing techniques with precise rotational control. Fan-in/fan-out (FIFO) devices are another major hurdle that needs to be developed. These components enable individual cores of a multi-core fiber to be connected to the single-mode fiber, but insertion loss can become a significant concern. In addition, FIFO devices may introduce unwanted polarization mode dispersion, which can further degrade overall system performance. Another challenge is the multi-core fiber amplifier. At present, multi-core EDFA technology is still not fully mature and remains an active area of research [50–53]. In long-haul communication systems, optical signals need to be periodically amplified to compensate for fiber attenuation. In conventional multi-core fiber transmission systems, where each core is typically amplified individually, the number of EDFAs scales with the number of cores. This leads to increased system complexity and higher cost per transmitted bit [54].

Fiber Type	**Strongly-Coupled MCF**		**Weakly-Coupled MCF**
	Systematically Coupled	**Randomly Coupled**	
Core pitch	Small	Medium	Large
Mode-coupling	Weak between supermodes	Strong and random	Weak and random over long distance
DGD scaling with distance	Linear	Square-root (sub-linear)	Linear

Table 2.1: Classification of multi-core fibers based on coupling regime [55].

2.3 Mode Coupling in Multi-Core Fibers

The modes in an optical fiber are the allowed spatial field distributions that are solutions of the wave equation and satisfy the appropriate boundary conditions [56]. An optical fiber supports a number of guided modes, commonly referred to as LP_{mn} modes. Here, LP_{mn} stands for linearly polarized modes, while m (azimuthal index) and n (radial index) describe the spatial intensity profile of light. The intensity distribution of the LP_{01} mode (also called the fundamental mode) is characterized by a single, centrally located circular intensity spot with a Gaussian-like decay away from the center. The LP_{11} mode exhibits a two-lobe structure resembling an hourglass shape, while the LP_{21} mode consists of four lobes forming a cross-like pattern. In addition, optical fibers also support a continuum of unguided radiation modes.

Coupling in an optical fiber refers to the transfer of optical power from one core to another. When light propagates in an optical medium such as a waveguide or optical fiber, it remains confined to the same core or mode. However, under certain conditions, some of the optical power can couple into another mode (mode-coupling) or into a neighboring core in a coupled-core multi-core fiber [57]. As the cores in coupled MCFs are placed close to each other, light in one core interacts with neighboring cores, resulting in periodic energy transfer between them.

When two identical waveguides are placed sufficiently close to each other, the optical mode confined in one waveguide extends beyond its core in the form of an evanescent field. If the separation between the waveguides is small enough, the evanescent fields overlap in the transverse cross-section of the structure. This overlap enables optical power to transfer from one waveguide to the other known as evanescent coupling. Mathematically, the coupling strength between two cores is determined by the overlap integral of the electric fields of the corresponding modes in the two cores. The strength of this interaction is quantified by the coupling coefficient, C, which is given by

$$C \sim \frac{\beta}{2} \iint E_1^*(x, y)\, E_2(x, y)\, dx\, dy, \tag{2.1}$$

where β is the propagation constant of the guided mode, and $E_1(x, y)$ and $E_2(x, y)$ are the normalized transverse electric-field distributions of the modes supported by the two waveguides. The symbol $(\cdot)^*$ denotes the complex conjugate, and the integration is done over the entire transverse cross-section. The overlap integral measures the spatial similarity of the two modal fields. A larger overlap corresponds to stronger coupling and more efficient power transfer between the waveguides, whereas a smaller overlap results in weaker coupling. Since the evanescent field decays exponentially away from the waveguide core, the coupling coefficient decreases rapidly as the separation between the waveguides increases.

In the linear regime, the propagation of light in coupled MCFs is determined by chromatic dispersion and inter-core coupling effects [58]. The transfer of optical power between cores arises from evanescent-field overlap and depends sensitively on the fiber geometry and material parameters. External effects such as mechanical bending, twisting, and thermal variations locally perturb the refractive-index profile, which lead to fluctuations in the coupling strength. These perturbations cause rapid decorrelation of modal fields in randomly-coupled multi-core fibers giving rise to statistically varying optical fields over time and frequency.

2.3.1 Ideal Mode Coupling

Ideal mode coupling refers to the deterministic and well-defined transfer of optical power between adjacent cores of a coupled-core multi-core fiber. The evolution of the optical field in each core is governed by a system of coupled differential equations described by coupled-mode theory (CMT), where the coupling coefficients are functions of the optical frequency, refractive index, and core spacing.

In strongly-coupled MCFs, the propagation of the optical field is described by the supermodes, which are approximately linear combinations of the guided modes of the individual cores. The supermodes are the collective field distributions of the entire coupled system and are characterized by their unique propagation constants. The dynamics of light inside the fiber are then governed by the interference between these supermodes. In an ideal coupled MCF, these supermodes are exact eigenmodes of the coupled system. Therefore, they are mutually orthogonal to each other and propagate independently without energy exchange. For example, consider two systematically-coupled identical waveguides. When optical power is injected into one of the cores to excite the local mode of that core, the optical power is periodically exchanged between the cores. In this case, the sinusoidal distribution of optical power in the linear regime results from inter-core coupling between the cores, as shown in Fig. 2.3(a). In the supermode picture, this excitation is equivalent to the simultaneous excitation of the even and odd supermodes. Each eigenmode propagates independently with its own propagation constant, and the power transfer between the cores arises from coherent beating between the supermodes rather than coupling between them.

Efficient power transfer between the cores occurs only when the modes are phase-matched. When the propagation constants are sufficiently far from each other (phase-mismatched), the coupling between the cores is reduced, resulting in less power transfer. The phase-matching condition depends on the propagation-constant difference, $\Delta\beta$, between the supermodes, with the coupling period being inversely proportional to $\Delta\beta$. Phase matching is achieved when $\Delta\beta$ is sufficiently small.

Coupled-Mode Theory for MCF

The interaction between the local modes of the individual cores is described by coupled-mode theory. Let the propagation of the modal field amplitudes in an N-coupled-core fiber be given by the vector

$$\mathbf{A}(z) = (A_1(z), A_2(z), \ldots, A_N(z))^T, \tag{2.2}$$

where $A_k(z)$ denotes the complex field amplitude in the k-th core. The coupled-mode equations can then be written as

$$\frac{d\mathbf{A}}{dz} = i\mathbf{M}\mathbf{A}, \tag{2.3}$$

where $\mathbf{M}$ is the $N \times N$ coupling matrix (and $2N \times 2N$ with polarization degeneracy of each mode) that governs the mode propagation and coupling dynamics of the coupled MCF [59]. For a system of identical coupled-cores, the matrix $\mathbf{M}$ can be expressed as

$$\mathbf{M} = \begin{bmatrix} \beta_0 & C_{12} & C_{13} & \cdots & C_{1N} \\ C_{21} & \beta_0 & C_{23} & \cdots & C_{2N} \\ C_{31} & C_{32} & \beta_0 & \cdots & C_{3N} \\ \vdots & \vdots & \vdots & \ddots & \vdots \\ C_{N1} & C_{N2} & C_{N3} & \cdots & \beta_0 \end{bmatrix}, \tag{2.4}$$

where β_0 denotes the propagation constant of the mode in an individual core, and C_{ij} represents the coupling coefficient between cores i and j. Under the weakly guiding approximation for a step-index fiber, the coupling coefficient between the i-th core and the j-th core (or mode) is given by [60, 61]

$$C_{ij} = \sqrt{\frac{n_1^2 - n_2^2}{n_1^2}} \cdot \frac{1}{r} \cdot \frac{U^2}{V^3} \cdot \frac{K_0(Wd/r)}{K_1^2(W)} \tag{2.5}$$

where n_1 and n_2 are the refractive indices of the core and cladding, respectively, r is the core radius, d is the core pitch, K_0 and K_1 are the modified Bessel functions of the second kind and of order 0 and 1, respectively, and V is the normalized frequency given by

$$V = \frac{2\pi r}{\lambda}\sqrt{n_1^2 - n_2^2}. \tag{2.6}$$

Together with $U \cdot K_0(W) \cdot J_1(U) = W \cdot K_1(W) \cdot J_0(U)$ and $U^2 + W^2 = V^2$, where $J_0(U)$ and $J_1(U)$ are the Bessel functions of the first kind of order 0 and 1, respectively, the coupling coefficients C_{ij} can be solved to express the supermodes as eigenmodes of the coupled MCF [62]. For example, Figure 2.2 shows the supermodes as linear combinations of eigenmodes for a dual coupled-core fiber (2CCF) and a four coupled-core fiber (4CCF). Since the coupling depends on the V parameter, the coupling is intrinsically frequency-dependent.

For an ideal MCF, $\mathbf{M}$ is a Hermitian matrix and can be diagonalized by a unitary matrix $\mathbf{Q}$ such that

$$\mathbf{Q}^{-1}\mathbf{M}\mathbf{Q} = \mathbf{\Lambda}, \tag{2.7}$$

where $\mathbf{\Lambda}$ is a diagonal matrix whose elements are the eigenvalues (propagation constants of the supermodes),

$$\mathbf{\Lambda} = \mathrm{diag}(\beta_1, \beta_2, \ldots, \beta_N). \tag{2.8}$$

and $\mathbf{Q}$ corresponds to the orthonormal eigenvectors of coupling matrix, $\mathbf{M}$. The field distribution of the supermodes can be written as [63]

$$\mathbf{B} = \mathbf{Q}^{-1}\mathbf{A}, \tag{2.9}$$

ans. the coupled-mode equation is transformed into a supermode (eigenmode) basis as

$$\frac{d\mathbf{B}}{dz} = i\mathbf{\Lambda}\mathbf{B}. \tag{2.10}$$

Thus, the amplitude of each supermode evolves independently as

$$B_m(z) = B_m(0)\, e^{i\beta_m z}, \tag{2.11}$$

where $B_m(z)$ is the amplitude of the m^{th} supermode at position z, $B_m(0)$ is the initial amplitude, and β_m is the propagation constant. It shows that in the supermode basis, each mode propagates independently without exchanging power with other modes.

Based on supermode analysis, two identical coupled waveguides support symmetric and antisymmetric eigenmodes with propagation constants β_1 and β_2, respectively. The propagation constants are given by

$$\beta_1 = \beta_0 + C, \qquad \beta_2 = \beta_0 - C, \tag{2.12}$$

where β_0 is the propagation constant of an individual core and C is the coupling coefficient between the two cores. For a four coupled-core

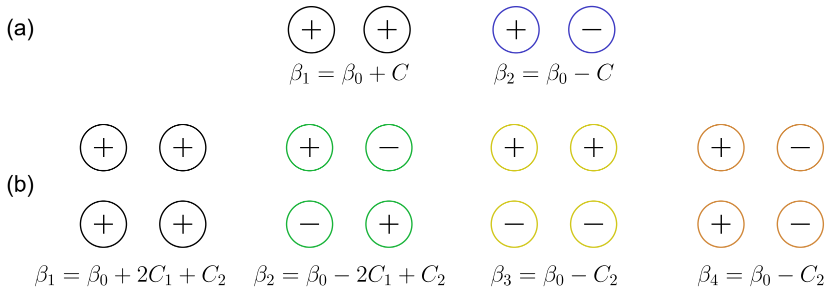

Figure 2.2: Schematic representation of the supermode in (a) a dual coupled-core fiber and (b) four coupled-core fiber. The symbols (+) and (-) indicate the relative phase of the optical field in each core.

fiber, there are four eigenvalues, two of which are degenerate. These eigenvalues are given by

$$\begin{aligned} \beta_1 &= \beta_0 + 2C_1 + C_2, \qquad & \beta_3 &= \beta_0 - C_2, \\ \beta_2 &= \beta_0 - 2C_1 + C_2, \qquad & \beta_4 &= \beta_0 - C_2, \end{aligned} \tag{2.13}$$

where C_1 and C_2 are the coupling coefficients between adjacent and non-adjacent cores, respectively.

Spatial modal dispersion (SMD) in a coupled-core fiber arises because the guided supermodes have different propagation constants, $\beta_m(\omega)$. Consequently, each supermode has a different group delay per unit length τ'_m, which is given by

$$\tau'_m = \frac{\partial \beta_m}{\partial \omega} = \frac{1}{v_{g,m}}, \tag{2.14}$$

where $v_{g,m}$ is the group velocity of the m^{th} supermode. After propagation over a fiber length L, the group delay of the supermode is

$$\tau_m = L \frac{\partial \beta_m}{\partial \omega}. \tag{2.15}$$

Therefore, the differential group delay (DGD) between two supermodes m and n is [62]

$$\Delta\tau_{mn} = L \left(\frac{\partial \beta_m}{\partial \omega} - \frac{\partial \beta_n}{\partial \omega} \right). \tag{2.16}$$

When a signal excites several supermodes simultaneously, these supermodes arrive at the fiber output at different times. This relative delay causes temporal pulse broadening and is referred to as spatial modal dispersion. A larger difference between the frequency derivatives of the supermode propagation constants results in a greater differential group delay and, consequently, stronger spatial modal dispersion. Degenerate supermodes have identical propagation constants and, ideally, identical group delays; therefore, they do not have a differential delay between each other.

For a dual coupled-core fiber, the group delays of the two supermodes after propagation over a length L are

$$\tau_1 = L\frac{\partial \beta_1}{\partial \omega} = L\left(\frac{\partial \beta_0}{\partial \omega} + \frac{\partial C}{\partial \omega}\right), \tag{2.17}$$

and

$$\tau_2 = L\frac{\partial \beta_2}{\partial \omega} = L\left(\frac{\partial \beta_0}{\partial \omega} - \frac{\partial C}{\partial \omega}\right). \tag{2.18}$$

Therefore, the differential group delay between the two supermodes is

$$\Delta\tau = \tau_1 - \tau_2 = 2L\frac{\partial C}{\partial \omega}. \tag{2.19}$$

The spatial modal dispersion is governed by the frequency dependence of the coupling coefficient. A constant C leads to a constant separation between the supermode propagation constants but no differential group delay, whereas a frequency-dependent C results in spatial modal dispersion.

Coupling Length

The coupling length represents the shortest propagation distance over which all optical power launched into one core is transferred to an adjacent core. Using supermode theory, the coupling length can be expressed as [64]

$$L_c = \frac{\pi}{\beta_1 - \beta_2} = \frac{\pi}{2C} \tag{2.20}$$

It is inverse of the coupling coefficient. The coupling length in weakly and strongly-coupled multi-core fibers is on the order of a few kilometers and a few hundred meters, respectively. For two coupled waveguides with symmetric cores, the coupling coefficients are equal, i.e., $C_{12} = C_{21}$. From Eq. (2.5), it can be seen that the coupling coefficient decreases as the separation between the waveguides increases. The variation of coupling length with frequency and normalized separation D is shown in Fig. 2.3(b). Here, $D = d/r$ is the normalized separation between two waveguides.

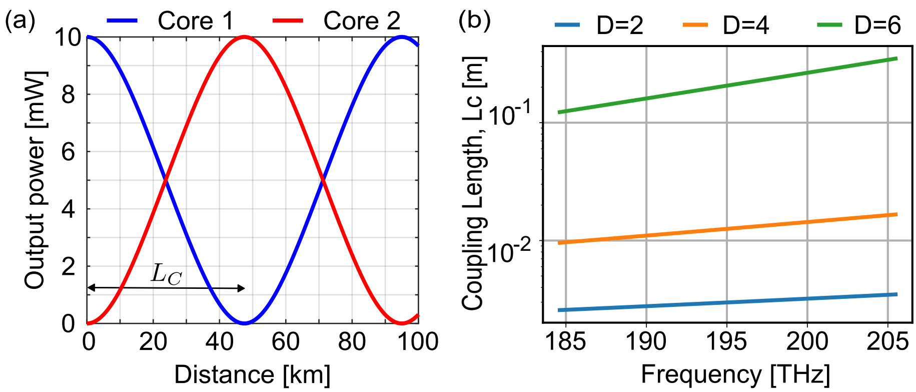

Figure 2.3: (a) Sinusoidal coupling of optical power in two identical coupled waveguides, and (b) variation of the coupling length with frequency and normalized separation D (see Eq. 2.5) between the two waveguides.

2.3.2 Random Mode Coupling

Unlike an ideal (unperturbed) multi-core fiber, a real MCF has imperfections that can originate from fabrication imperfections and environmental perturbations. These perturbations induce random fluctuations in the coupling in both the time and frequency domains.

Environmental perturbations mainly arise from variations in surrounding temperature, acoustic vibrations, and fiber bending and twisting. Mechanical stress and strain, including macrobending and microbending, can also physically affect the fiber. These external perturbations can degrade optical fiber performance by altering the properties of the fiber, such as its refractive index and attenuation, as well as the properties of the propagating light, including its phase and state of polarization (SOP). Fabrication imperfections in multi-core fibers arise from inherent deviations and errors during the manufacturing process. These include variations in core geometry such as core-diameter and core-eccentricity, core-pitch fluctuations, refractive-index variations, and structural asymmetries along the fiber length. In addition, non-uniform stress induced in MCFs during the fiber drawing process can also affect the optical properties.

In coupled-core multi-core fibers, optical power is transferred efficiently only when the propagation constants of the cores are phase matched. Inefficient coupling in real MCFs can happen due to phase mismatch induced by imperfections. The randomness of the coupling arises from the random distribution of these imperfections along the fiber.

Such a non-ideal fiber geometry leads to variations in the propagation constants and fluctuations in the coupling coefficients along the fiber. As a result, the symmetry of the multi-core fiber is broken which causes performance degradation such as increased crosstalk, differential group delay spread, and mode dependent loss. These structural imperfections may also induce random birefringence, resulting in polarization-mode dispersion (PMD) and polarization crosstalk. These perturbations in optical fibers also cause group-delay mismatches between the supermodes, which typically dominate the overall impulse response of the coupled system.

Transfer Matrix Representation of Mode Coupling

The propagation of optical fields in a multi-core fiber can be conveniently described using a transfer matrix formalism. Instead of the continuous evolution of modal amplitudes along the propagation direction z, the system is represented as a linear input-output relation between the complex modal field vectors at the fiber input and output as

$$\mathbf{A}_{\text{out}} = \mathbf{T}(\omega, t) \cdot \mathbf{A}_{\text{in}}, \tag{2.21}$$

where, column vectors $\mathbf{A}_{\text{in}}$ and $\mathbf{A}_{\text{out}}$ represent the complex modal amplitudes (or core fields) at the input and output of the fiber, respectively. The frequency and time-dependent transfer matrix, $\mathbf{T}(\omega, t)$, fully describes the linear propagation of the optical fields and captures slow variations induced by environmental effects such as temperature fluctuations, mechanical stress, and fiber bending. The general form of the transfer matrix for an N-core MCF can be written as

$$\mathbf{T}(\omega, t) = \begin{pmatrix} m_{11}(\omega, t) & m_{12}(\omega, t) & \cdots & m_{1N}(\omega, t) \\ m_{21}(\omega, t) & m_{22}(\omega, t) & \cdots & m_{2N}(\omega, t) \\ \vdots & \vdots & \ddots & \vdots \\ m_{N1}(\omega, t) & m_{N2}(\omega, t) & \cdots & m_{NN}(\omega, t) \end{pmatrix}, \tag{2.22}$$

where each element $m_{ij}(\omega, t)$ represents the complex field transfer coefficient from the j^{th} input core to the i^{th} output core. The diagonal elements of the transfer matrix, m_{ii}, describe field transmission and propagation loss within the same core, while the off-diagonal terms m_{ij} $(i \neq j)$ represent inter-core coupling induced by evanescent field overlap and perturbations along the fiber.

The frequency dependence of the transfer matrix comes from the fact that optical propagation is inherently dispersive. The refractive index $n(\omega)$ of the optical fiber is frequency dependent and described by the Sellmeier equation [65], which describes material dispersion in the optical medium. During propagation, different optical frequencies accumulate different phase shifts, $\beta(\omega) = n(\omega) \cdot \omega/c$. The structure of the waveguide (core and cladding geometry) also contributes to making the propagation constant frequency dependent. In coupled-core multi-core fibers, the coupling is inherently frequency dependent, as described in Section 2.3. Since the coupling coefficients also depend on frequency, the coupling matrix becomes frequency dependent, and consequently so does the transfer matrix [66].

The explicit time dependence of the transfer matrix, $\mathbf{T}(\omega, t)$, arises from changes in the optical properties of the fiber over time, such as variations in the refractive index due to the thermo-optic effect and thermal expansion, as well as slight deformations of the fiber caused by mechanical stress and strain, as discussed above. These random perturbations induce slow temporal drifts in the effective propagation constants and coupling coefficients. As a result, even under stationary excitation of the input core, the output fields evolve slowly with time.

It is important to distinguish between the two time scales that appear in the transfer matrix formulation. In transfer matrix $T(\omega, t)$, the variable ω denotes the optical angular frequency and describes the spectral response of the multi-core fiber, whereas t represents a slow time variable that captures the temporal evolution of the fiber caused by environmental perturbations such as temperature fluctuations, mechanical stress, and bending. This dependence reflects the fact that the propagation constants and coupling coefficients are not strictly static, but drift slowly with time as the physical state of the fiber changes. Since $T(\omega, t)$ is defined in the frequency domain, the corresponding time-domain representation is obtained by taking the inverse Fourier transform with respect to ω. The resulting matrix impulse response can be written as

$$H(\tau, t) = \mathcal{F}^{-1}_{\omega \to \tau} T(\omega, t), \tag{2.23}$$

where τ denotes the fast time (or delay) variable associated with optical signal propagation and should not be confused with the slow environmental time variable t. The solution of the coupled-mode equation in Eq. 2.3 can also be expressed as

$$\mathbf{T}(\omega, t) = \exp\left\{ i\, \mathbf{M}(\omega, t) z \right\}. \tag{2.24}$$

Thus, the transfer matrix representation of CMT provides a powerful way to analyze time-varying random perturbations and random coupling

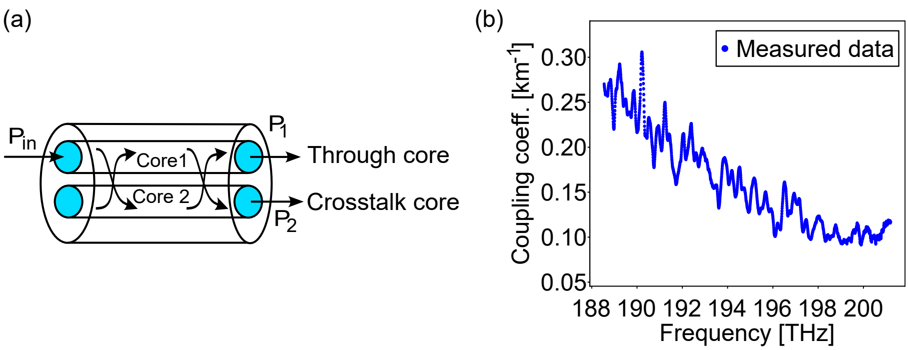

Figure 2.4: Illustration of (a) optical power launched into one core being redistributed among neighboring cores due to inter-core coupling, and (b) the measured frequency dependence of the inter-core coupling coefficients.

dynamics in a coupled-core multi-core fiber links. It is very convenient to use the matrix representation to study the statistical properties of random power fluctuations and crosstalk behavior in coupled MCFs, as done in paper [B].

2.4 Impairments in MCF Systems

Several physical impairments limit the performance of the multi-core fiber systems, including inter-core crosstalk, differential group delay (DGD), mode coupling and random mode mixing, mode-dependent loss (MDL) and polarization-related impairments such as polarization mode dispersion. These effects degrade overall channel transmission performance. In this section, we discuss each of the impairments that occur in the coupled-core multi-core fiber systems.

2.4.1 Inter-core Crosstalk

Crosstalk refers to unwanted leakage of optical power between cores or modes and constitutes a fundamental limitation in the multi-core fiber transmission, particularly in high-capacity optical communication systems [67]. It is defined as the ratio of the output power leaked into the adjacent core to the output power remaining in the launched core, where the power is injected [68]. Mathematically, it is expressed as

$$XT = \frac{P_2}{P_1}, \tag{2.25}$$

where P_2 is the measured output power in the neighboring core due to inter-core coupling, and P_1 is the optical power remaining in the excited core, as shown in Fig. 2.4(a).

In weakly-coupled homogeneous multi-core fibers, structural perturbations such as bending and twisting cause longitudinal variations in the local propagation constants of the cores. As a result, inter-core crosstalk is generated mainly at randomly distributed phase-matching points, where the propagation constants of adjacent cores become locally phase matched [69, 70]. The total crosstalk is the cumulative sum of the crosstalk contributions at these phase-matching points, weighted by the random phase shifts and propagation delays along the optical fiber. As a result, the crosstalk appears as a noise-like optical signal with random amplitude and phase characteristics. The intrinsic frequency dependence of the coupling causes the crosstalk signal to depend on the frequency, as shown in Fig. 2.4(b).

2.4.2 Group Delay Spread

In optical fibers, the frequency dependence of the refractive index causes different colors of light to travel at different speeds, resulting in time delays. The group delay (GD), τ_q is defined as the time delay experienced by different frequency components of an optical signal as they propagate through an optical fiber. The GD of the q-th principal propagation mode at each frequency is equal to the negative slope of its phase response, $\phi_q(\omega)$ with respect to that frequency.

$$\tau_q = -\frac{\partial \phi_q(\omega)}{\partial \omega}. \tag{2.26}$$

The broadening of the pulse in the time domain leads to signal degradation in high-capacity communication systems.

The group delay spread (GDS), σ_τ in a strongly-coupled multi-core fiber is the standard deviation of the group delays associated with the principal propagation modes [71]. It measures the temporal dispersion of modes by quantifying the variation in their propagation times. Mathematically, the GDS can be calculated as [72]

$$\sigma_\tau = \sqrt{\frac{1}{N}\sum_{q=1}^{N} \tau_q^2}, \tag{2.27}$$

where the group delay τ_q corresponds to the eigenvalues of the group delay operator $D(\omega)$. The group delay operator is defined as

$$D(\omega) \equiv T(\omega)^{-1} \frac{\partial T(\omega)}{\partial \omega} \tag{2.28}$$

$T(\omega)$ represents the frequency-dependent transfer matrix describing inter-core coupling in the multi-core fiber, and the eigenvalues τ_q is the group delays of the principal states (supermodes) of the MCF link. In multi-core fibers, different cores experience different group delays due to fabrication variations and coupling effects, leading to group delay spread (GDs), which is a key impairment in high-capacity transmission system.

Another metric that quantifies the delay between principal polarization modes is the differential group delay (DGD). Each spatial mode of an optical fiber supports two orthogonal polarization states. In a birefringent medium, these orthogonal polarization modes propagate at different speeds due to random birefringence of the optical fiber, which introduces a relative delay between them. The difference in propagation delay between the two polarization modes is known as the differential group delay. It quantifies the strength of polarization-mode dispersion (PMD) per unit length.

To compensate for the relative delays between polarization states in a multi-core fiber transmission system, MIMO DSP employs adaptive equalizers. The computational complexity of the MIMO DSP is proportional to the DGD, as larger delays require a greater number of equalizer taps to effectively compensate for the resulting temporal dispersion [73]. The DGD is directly related to the width of the impulse response function (i.e., the temporal response of the channel when an ideal Dirac delta impulse is launched at the input) of the system.

2.4.3 Mode-dependent Loss

In a strongly-coupled multi-core fiber, light propagates through different spatial paths (super-modes). These modes may experience different levels of attenuation due to fiber bending and imperfections. Mode-Dependent Loss (MDL) in multi-core fibers quantifies the variation in optical attenuation among different spatial modes or cores. MDL effectively reduces the number of propagating modes, resulting in a proportional decrease in overall channel capacity and data rates. In randomly-coupled multi-core fibers, complete mode mixing reduces the accumulation of MDL from being linear with distance to scaling with the square root of the propagation distance [74].

In an ideal SDM system without MDL, the transfer matrix is unitary. Therefore, MDL leads to a non-unitary channel transfer matrix and, when combined with mode mixing, results in signal distortion and noise enhancement, which reduces the overall system capacity [75]. The effects of MDL are commonly mitigated using MIMO DSP combined with specialized MDL equalization techniques, such as long-period gratings, which selectively attenuate specific modes more than others in order to balance the loss across all channels. For the strongly coupled regime, the MDL of an SDM system is defined as

$$\mathrm{MDL_{dB}} = 20 \cdot \log_{10}\left(\frac{|\lambda_{max}|}{|\lambda_{min}|}\right), \tag{2.29}$$

where λ_{max} and λ_{min} denote the largest and smallest eigenvalues obtained from the singular value decomposition of the measured transfer matrix, respectively. In a dual-polarization single-mode system, MDL is equivalent to polarization-dependent loss (PDL).

Chapter 3

Nonlinear Interactions in Coupled MCFs

There are several nonlinear effects that occur in optical fibers. In this chapter, we will mainly focus on wavelength conversion based on four-wave mixing process and nonlinear coupling due to self-phase modulation in coupled-core multi-core fibers. The efficiency of wavelength conversion strongly depends on the phase-matching condition. As the phase mismatch accumulates along fiber length, the effect of coupling strength on the phase matching condition becomes an important parameter to consider, which is briefly discussed. When working with high power, optical power back reflection from optical fiber becomes a critical issue, so we need to mitigate it by suppressing stimulated Brillouin scattering (SBS), and methods for increasing the SBS threshold are also presented in this chapter. In the last section, we discuss the effect of modal dispersion on four-wave mixing efficiency.

3.1 Stimulated Brillouin Scattering

Stimulated Brillouin Scattering is a nonlinear scattering phenomenon in optical fibers that arises from the interaction of light with acoustic phonons in silica. Along with Stimulated Raman Scattering (SRS), it is one of the major nonlinear effects in optical fibers. Unlike SRS, which involves optical phonons (quantized vibrational modes) and can occur in both forward and backward directions, SBS predominantly generates backward-scattered light. The Stimulated Brillouin Scattering occurs through the process of electrostriction, where the optical field creates periodic density variations in the fiber. These density variations form an acoustic wave that acts as a moving grating, scattering the incident light backward and producing a frequency-shifted Stokes wave. As the Stokes wave grows, it strengthens the acoustic wave, resulting in enhanced backscattering [76] and efficient power transfer from the pump light to the Stokes light. In contrast, the anti-Stokes wave is generated when the scattered photons gain energy from the acoustic phonons, resulting in a frequency higher than that of the pump wave as shown in Fig. 3.1. Its intensity is typically weaker because this process requires the annihilation of thermally excited phonons, which are less populated under normal conditions. The emission of the anti-Stokes wave is typically weaker than that of the Stokes wave [77].

The SBS threshold is the input power level at which the Stokes wave power increases rapidly and becomes comparable to the pump power [78]. Once the Brillouin threshold is reached, most of the input optical power is carried away by backward-propagating Stokes waves. Because SBS efficiently reflects optical power back toward the source, it is one of the important nonlinear effects limiting power transmission in narrow-linewidth optical systems and high-speed long haul-optical communication networks [79]. The SBS threshold strongly depend on the fiber length, as longer fibers reduce the threshold power due to increased interaction length. As a result, SBS becomes more significant in long optical fibers than in short-reach optical fibers.

Quantum mechanically, SBS can be viewed as a scattering process in which the annihilation of an incident photon simultaneously creates a scattered photon (or Stokes photon) and an acoustic phonon. The conservation of energy and momentum of the interacting quanta leads to relations between the frequency and wave vector of the incident photon, the Stokes photon, and the acoustic phonon, which are given by [80]

$$\Omega_B = \omega_p - \omega_s, \qquad \mathbf{k}_A = \mathbf{k}_p - \mathbf{k}_s \tag{3.1}$$

where ω_p and ω_s are the frequencies, and $\mathbf{k}_p$ and $\mathbf{k}_s$ are the wave vectors of the incident pump photon and the back-scattered Stokes wave, respectively. The frequency Ω_B and wave vector $\mathbf{k}_A$ of the acoustic phonon satisfy [77]

$$\Omega_B = \nu_A|\mathbf{k_A}| \approx 2\nu_A|k_p|\sin(\theta/2), \tag{3.2}$$

where ν_A is the velocity of the acoustic phonon. The efficiency of Brillouin scattering strongly depends on the angle θ between the incident

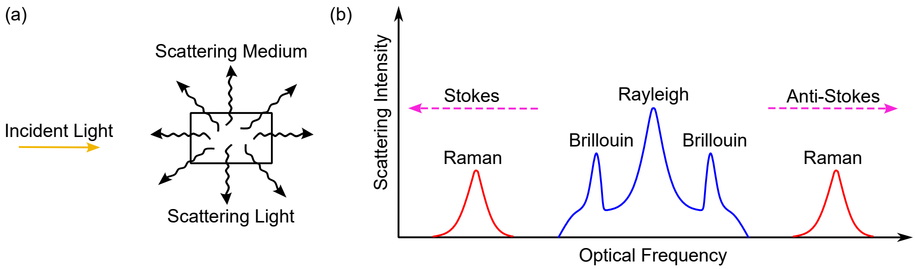

Figure 3.1: (a) Schematic illustration of light scattering from a scattering medium. (b) Frequency-domain representation of the scattered light, showing the stimulated Brillouin scattering signal and Raman-scattered light components relative to the incident optical frequency.

pump and Stokes waves. The frequency shift Ω_B is maximum in the backward direction ($\theta = \pi$) and approaches zero in the forward direction ($\theta = 0$). As optical fibers support only forward and backward propagating guided modes, SBS predominantly occurs in the backward direction due to phase-matching conditions.

The Brillouin-gain spectrum describes the frequency variation of SBS gain, which peaks at the Brillouin shift Ω_B. The narrow Brillouin linewidth is determined by the short lifetime (typically less than 10 ns) of the acoustic phonon, which leads to a Lorentzian-shaped gain profile of the form [80]

$$g_B(\Omega) = \frac{g_p(\Gamma_B/2)^2}{(\Omega - \Omega_B)^2 + (\Gamma_B/2)^2}. \tag{3.3}$$

The peak value of the Brillouin gain at $\Omega = \Omega_B$ is given by [80]

$$g_p = \frac{4\pi^2\gamma_e^2 f_A}{n_p c\lambda^2 \rho_0 \nu_A \Gamma_B} \tag{3.4}$$

where γ_e is the electrostrictive constant of silica, f_A is the acoustic-optical mode overlap factor, n_p is the refractive index of the fiber at the pump wavelength, c is the speed of light in vacuum, λ is the pump wavelength, ρ_0 is the material density of silica, ν_A is the acoustic velocity, and Γ_B is the linewidth (full width at half maximum) of the Brillouin gain spectrum. The lifetime of the phonon is the inverse of the Brillouin linewidth. The Brillouin linewidth varies approximately as $1/\lambda^2$ with the pump wavelength, so the narrowing of the gain spectrum compensates for the reduction in gain. Hence, the peak Brillouin gain is

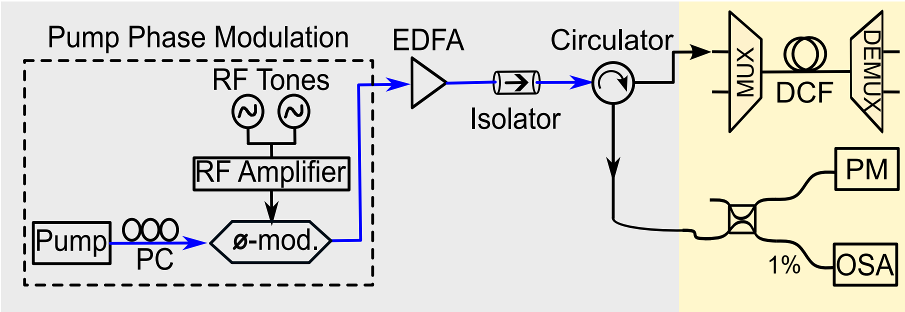

Figure 3.2: Schematic of the experimental setup for the measurement of stimulated Brillouin scattering in a dual coupled-core fiber.

nearly independent of the pump wavelength. The spectrum and peak gain also depend on fiber properties such as acoustic damping, material composition, and doping of the optical fiber.

Experimental Implementation

When high optical powers are transmitted through an optical fiber, stimulated Brillouin scattering can become significant. Once the SBS threshold is exceeded, a large portion of the launched optical power may be backscattered unless appropriate mitigation techniques are employed. Therefore, it is important to increase the SBS threshold to reduce the impact of SBS. Several techniques have been introduced for this purpose, such as the use of cascaded optical isolators to block the reflected light, applying a temperature gradient along the fiber, and increasing the spectral bandwidth of the input light. One such technique to increase the linewidth of the input light is phase modulation, which can be implemented using several sinusoidal tones [81]. Phase modulation with a single sinusoidal tone can theoretically achieve up to 4.8 dB of SBS suppression [82]. To achieve higher SBS suppression, multiple radio frequency (RF) tones with the required RF power can be used at the input of the phase modulator. These RF tones should be selected such that their frequencies do not overlap with any harmonic frequencies of each other. The frequency of the phase-modulating tones must be greater than the SBS bandwidth of the fiber under test.

In Paper [A], the pump phase modulation technique is used to suppress stimulated Brillouin scattering by broadening the optical spectrum of the pump laser. The experimental setup is shown in Fig. 3.2. It con-

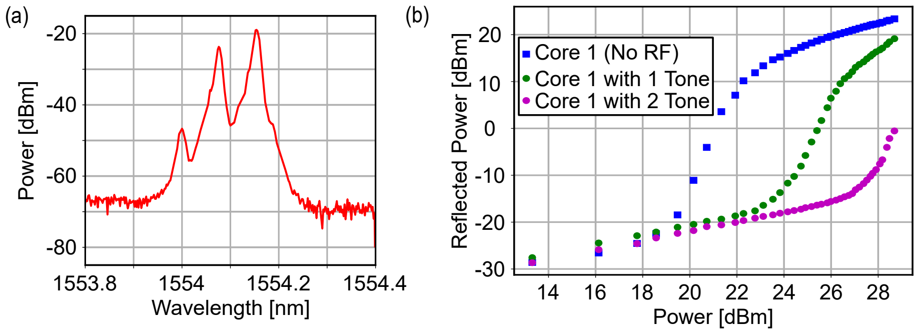

Figure 3.3: (a) Back-reflected power spectrum of the DCF, and (b) SBS threshold power measured with and without phase modulation.

sists of a tunable pump laser in C-band. The output of the pump laser is fed into a phase modulator. Since the phase modulator is sensitive to the state of polarization (SOP) of the input light, a polarization controller is used to align the input SOP before the phase modulator to achieve optimum output power. The electrical drive signals for the phase modulator are generated using RF generator. The generated RF tones also contain higher-order sidebands, which are undesirable. An RF filter is used to remove these unwanted higher-order RF components. Phase modulation does not directly change the optical power; instead, it modulates the instantaneous phase of the optical field. As a result, the optical frequency becomes time-dependent, leading to the generation of frequency sidebands around the original carrier. This process effectively broadens the optical spectrum of the laser. When two RF tones centered around 95 MHz and 305 MHz are applied, the phase modulator imposes a multi-tone modulation pattern on the optical signal. This results in a comb-like spectrum containing multiple frequency components. Consequently, the pump power is distributed over a wider bandwidth, which reduces the effective spectral power density.

The RF tones are amplified using an RF amplifier before being applied to the phase modulator. The phase-modulated optical signal is then amplified using a high-power EDFA and launched into a dual-core fiber (DCF) through an optical circulator. The back-reflected light generated by SBS is recorded using an optical spectrum analyzer and a power meter. An optical isolator is used in the setup to prevent high-power back-reflected light from the dual-core fiber from reaching the laser source, thereby protecting the pump laser from potential damage.

The SBS threshold power can be measured by sweeping the input pump power and simultaneously recording the total back-reflected power from the dual-core fiber. This can be done with the help of a circulator, which allows the back-reflected power from the DCF to be received by a power meter or an optical spectrum analyzer (OSA). The back-reflected power spectrum contains both Rayleigh and Brillouin peaks, as shown in Figure 3.3(a). The SBS threshold of core 1 of the dual-core fiber without phase modulation, with single RF tone (95 MHz) modulation, and with two RF tones (95 MHz and 305 MHz) modulation are shown in Figure 3.3(b). The SBS threshold of the pump increases from 18.5 dBm to 23 dBm and 27.5 dBm with one-tone and two-tone modulation, respectively.

3.2 Four-Wave Mixing

In the linear regime, propagation of optical fields is primarily governed by propagation loss and dispersion. The nonlinear interaction between light and matter in an optical medium, whose response is a nonlinear function of the electromagnetic field, can be described in terms of induced nonlinear polarization. The electric polarization field P of a nonlinear material is dependent on the applied electric field E as

$$\mathbf{P} = \epsilon_0 \left(\chi^{(1)}\mathbf{E} + \chi^{(2)}\mathbf{EE} + \chi^{(3)}\mathbf{EEE} + \dots \right), \tag{3.5}$$

where, ϵ_0 is the vacuum permittivity and χ is the electric susceptibility of the medium. For simplicity, assuming linearly polarized light and neglecting the tensor nature of the electric susceptibility, the nonlinear polarization can be written as [80]

$$\begin{aligned}\mathbf{P}_{\text{tot}}(\omega) = \epsilon_0\chi^{(1)}\mathbf{E}(\omega) + 2\epsilon_0\chi^{(2)}\mathbf{E}(\omega)\mathbf{E}(0) \\ +3\epsilon_0\chi^{(3)}|\mathbf{E}(\omega)|^2\mathbf{E}(\omega) + \cdots\end{aligned} \tag{3.6}$$

The second and third terms in Eq. 3.6 represent the nonlinear effects on the propagation of light in an optical medium. Optical fibers are made of silica, which is amorphous and possesses inversion symmetry. The $\chi^{(2)}$ nonlinearity vanishes in isotropic media and is practically zero in standard optical fibers. In such media, all second-order nonlinear processes are forbidden by symmetry. The $\chi^{(3)}$ material [83] enables nonlinear effects such as two-photon absorption [84, 85], third-harmonic generation [86,87], Kerr nonlinear refraction [88,89], and four-wave mixing [90–93]. When the optical medium is exposed to high-intensity laser light, the refractive index of the material starts to change. This intensity-dependent variation in the refractive index along the fiber is referred to as the Kerr effect (or Kerr nonlinearity). It is expressed as [94]

$$n = n_0 + n_2 I, \tag{3.7}$$

where n_0 is the linear (low-intensity) refractive index, n_2 is the nonlinear refractive index coefficient, and I is the optical intensity.

Four-wave mixing (FWM) is a third-order nonlinear optical process that arises from the Kerr nonlinearity of a medium, where optical waves interact to generate new frequency components. The main characteristics of FWM can be explained by the third-order nonlinear polarization term in Eq. 3.5. The interaction among four linearly polarized electric fields at frequencies ω_1, ω_2, ω_3, and ω_4, due to the third-order nonlinear polarization, can be expressed as [80]

$$P_{\text{3rd term}} = \frac{1}{2}\hat{x}\sum_{j=1}^{4} P_j \exp\{i(k_j z - \omega_j t)\} + c.c., \tag{3.8}$$

where k_j is the propagation constant of the j-th component of the electric field. P_j contains many terms consisting of products of electric fields, and one such term is

$$\begin{aligned} P_4 = \frac{3\epsilon_0}{4}\chi^{(3)}_{xxxx}\Big[&|E_4|^2 E_4 + 2\big(|E_1|^2 + |E_2|^2 + |E_3|^2\big)E_4 \\ &+2E_1E_2E_3e^{i\theta_1} + 2E_1E_2E_3^* e^{i\theta_2} + \cdots\Big] \end{aligned} \tag{3.9}$$

where,

$$\begin{aligned} \theta_1 &= (k_1 + k_2 + k_3 - k_4)z - (\omega_1 + \omega_2 + \omega_3 - \omega_4)t \\ \theta_2 &= (k_1 + k_2 - k_3 - k_4)z - (\omega_1 + \omega_2 - \omega_3 - \omega_4)t \end{aligned} \tag{3.10}$$

The first four terms describe self-phase modulation (SPM) and cross-phase modulation (XPM), while the remaining frequency-combinations represent four-wave mixing. The number of effective terms contributing to FWM depends on the phase-matching condition among them.

3.2.1 Phase Matching Condition

Quantum mechanically, FWM can be thought of as the annihilation of photon pairs to create new photon pairs at different frequencies, such that

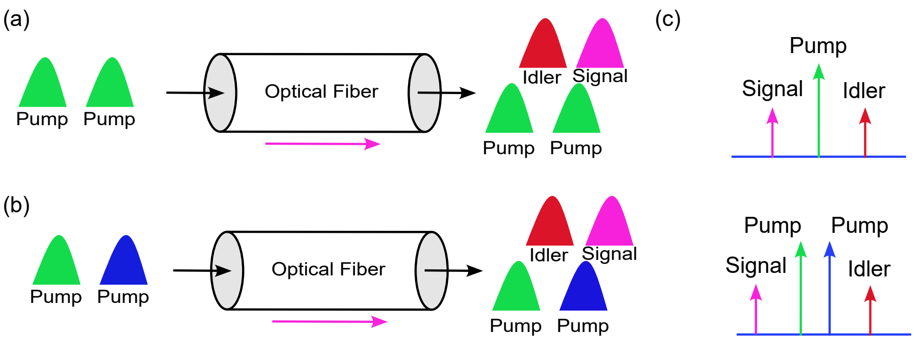

Figure 3.4: Schematic illustration of (a) degenerate and (b) nondegenerate four-wave mixing processes in an optical fiber, and (c) the corresponding four-wave mixing representation in the frequency domain [95].

energy and momentum are conserved. The terms in θ_2 correspond to the process in which two photons at frequencies ω_1 and ω_2 are annihilated to produce two new photons at frequencies ω_3 and ω_4 such that

$$\omega_1 + \omega_2 = \omega_3 + \omega_4, \tag{3.11}$$

and, the phase matching is given as

$$\Delta k = k_1 + k_2 - k_3 - k_4. \tag{3.12}$$

FWM is classified as degenerate and non-degenerate based on the frequencies of the interacting waves, as illustrated in Figure 3.4(a) and (b). When $\omega_1 = \omega_2$, only one pump is required to initiate FWM. This is called degenerate FWM. In this case, a strong pump at frequency ω_1 symmetrically generates two sideband frequencies ω_3 and ω_4, as shown in Fig. 3.4(c). Whereas, in the non-degenerate case, two pumps at frequencies ω_1 and ω_2 are required for FWM. The frequency detuning, Ω of the side bands are

$$\Omega = \omega_1 - \omega_3 = \omega_4 - \omega_2, \quad \omega_3 < \omega_1 < \omega_2 < \omega_4. \tag{3.13}$$

The lower-frequency sideband is referred to as the Stokes wave, whereas the higher-frequency sideband is called the anti-Stokes wave. They are also termed as the signal and idler, respectively. For the common degenerate case, where two pump photons at frequency ω_1 interact with a signal photon at ω_3, an idler is generated at [95]

$$\omega_4 = 2\omega_1 - \omega_3. \tag{3.14}$$

In this, the transfer of energy occurs from the pump to two sidebands that are frequency-shifted by Ω. With only one pump, the signal and idler can be generated from noise if the phase-matching condition is satisfied. On the other hand, when a weak signal is launched together with the pump into an optical fiber, an idler wave is generated while the signal is simultaneously amplified. This process is referred to as parametric amplification [96, 97], and the resulting gain is called parametric gain.

3.2.2 Wavelength Conversion in Multi-Core Fibers

The evolution of the slowly varying electric field envelopes A_1 and A_2 in two identical linearly coupled waveguides is governed by the coupled nonlinear Schrödinger equations (NLSEs) [98].

$$\begin{aligned}
\frac{\partial A_1}{\partial z} &= \underbrace{i\sum_{n=2}^{\infty}\frac{i^n\beta_n}{n!}\frac{\partial^n A_1}{\partial t^n}}_{\text{Dispersion}} + \underbrace{i\gamma A_1|A_1|^2}_{\text{Kerr nonlinearity}} + \underbrace{iCA_2}_{\text{Coupling}} - \underbrace{\frac{\alpha}{2}}_{\text{Loss}}A_1, \\
\frac{\partial A_2}{\partial z} &= i\sum_{n=2}^{\infty}\frac{i^n\beta_n}{n!}\frac{\partial^n A_2}{\partial t^n} + i\gamma A_2|A_2|^2 + iCA_1 - \frac{\alpha}{2}A_2.
\end{aligned} \tag{3.15}$$

Here, the first term represents the dispersion effect in the optical fiber, where β_n are the dispersion coefficients and the summation accounts for higher-order dispersion effects. The second term describes the nonlinear contribution arising from the Kerr effect, where γ is the nonlinear coefficient of the fiber and the term accounts for self-phase modulation. The third term present in the equation represents the coupling between the two cores, where C is the coupling strength that governs power exchange along the propagation direction. The last term accounts for propagation loss, where α is the attenuation coefficient of the fiber.

To achieve efficient wavelength conversion (high conversion efficiency with wide bandwidth) based on parametric interaction, the following conditions should be satisfied [95]:

(a) The pump wavelength should be near the zero-dispersion wavelength (ZDW);

(b) variations in chromatic dispersion (β_2 and β_4 coefficients) along the fiber length should be minimum; and

(c) pump and signal must have the same polarization state.

The coupled NLSEs (Eq. 3.15) are numerically solved using the split-step Fourier method (SSFM). In this method, the linear and nonlinear operators are defined as [98]

$$D_k = i\sum_{n=2}^{\infty} i^n \frac{\beta_n}{n!}\frac{\partial^n}{\partial t^n} - \frac{\alpha}{2}, \quad N_k = i\gamma|u_k|^2.$$

Where, k represents the core index. The output fields $A_1(z+dz)$ and $A_2(z+dz)$ at each propagation step dz are obtained by first applying the dispersion and nonlinear operators to each core independently over a half step, then applying the full nonlinear step, followed again by a half dispersion step, and finally the two fields are coupled using a 2x2 coupler transfer matrix $R(dz)$, neglecting the linear and nonlinear operators. The coupler matrix is defined as [99]

$$R(dz) = \begin{bmatrix} \cos(Cdz) & i\sin(Cdz) \\ i\sin(Cdz) & \cos(Cdz) \end{bmatrix}. \tag{3.16}$$

The numerical propagation of Eqs. 3.15 can be expressed in terms of the field evolution as

$$\begin{bmatrix} A_1(z+dz) \\ A_2(z+dz) \end{bmatrix} \approx R(dz) \begin{bmatrix} e^{D_1 dz/2} e^{N_1 dz} e^{D_1 dz/2} A_1(z) \\ e^{D_2 dz/2} e^{N_2 dz} e^{D_2 dz/2} A_2(z) \end{bmatrix}. \tag{3.17}$$

The solution is valid under the condition that the step size dz is much smaller than the characteristic coupling, nonlinear, and dispersion lengths of the dual coupled-core fiber.

The wavelength conversion efficiency (CE) is defined as the ratio of the idler output power to the input signal power. When only one core of the DCF is excited, the CE for core 1 and core 2 is given as

$$\mathrm{CE}_{\mathrm{core}_1} = \frac{|u_{i_1}(L)|^2}{|u_s(0)|^2} \quad \mathrm{CE}_{\mathrm{core}_2} = \frac{|u_{i_2}(L)|^2}{|u_s(0)|^2} \tag{3.18}$$

Here, $|u_{i_1}(L)|^2$ and $|u_{i_2}(L)|^2$ are the idler powers at position $z = L$ in core 1 and core 2, respectively, and $|u_s(0)|$ is the input signal power at $z = 0$. Under the undepleted pump approximation [94] for single mode fiber, the coupled equations can be solved analytically and one obtains [95]

$$\mathrm{CE} = \gamma^2 P_p^2 L^2 \,\mathrm{sinc}^2\left(gL\right), \tag{3.19}$$

The phase mismatch is defined as

$$\Delta\beta = 2\left(\frac{\beta_2}{2}\Omega^2 + \frac{\beta_4}{24}\Omega^4\right), \tag{3.20}$$

where β_2 and β_4 represent the second and fourth-order dispersion coefficients, respectively, and Ω denotes the frequency detuning. The nonlinear interaction is characterized by the gain parameter g as

$$g = \sqrt{\frac{1}{4}\Delta\beta\,(\Delta\beta + 4\gamma P_p)}, \tag{3.21}$$

where γ is the nonlinear Kerr coefficient and P_p is the pump power. It accounts for the combined influence of chromatic dispersion and nonlinear phase accumulation. In multicore or multimode fibers, optical fields propagate in different spatial modes or cores. Nonlinear interaction between them can lead to the generation of new frequency components through intermodal four-wave mixing, where phase matching between different modes or cores governs the efficiency of the process.

3.2.3 Experimental Implementation

Several wavelength conversion techniques have been proposed, among which parametric conversion based on optical fiber four-wave mixing offers two key advantages: (a) high conversion speed and (b) simultaneous conversion over a broad wavelength range.

In Paper [A], wavelength conversion in a highly nonlinear dual coupled-core fiber (DCF) is demonstrated. The schematic of the experimental setup is shown in Fig. 3.5(a). The setup consists of a pump and a tunable signal laser. The pump laser is phase modulated to suppress the effects of SBS in the coupled DCF, as explained earlier in Section 3.1. The phase-modulated pump is amplified using a high-power EDFA. An optical isolator is placed before the input of the WDM coupler to block back-reflected light from the DCF, which could otherwise damage the optical components. The strong pump with power of about 24 dBm is combined with a weak signal using a WDM coupler before launching into one of the cores of the DCF. In addition, the WDM coupler helps filter out the unwanted amplified spontaneous emission (ASE) noise generated by the high-power EDFA during the amplification process. The DCF output is recorded using an OSA through a 1% tap coupler, while a power meter is used to monitor the total output power.

As we have seen, the coupling is wavelength dependent and varies randomly due to geometric imperfections in the coupled-core multi-core fiber. The aim of this experiment is to understand the behavior of idler power transfer from one core to another when only one core is excited. Since the input signal wavelength is swept to investigate the wavelength

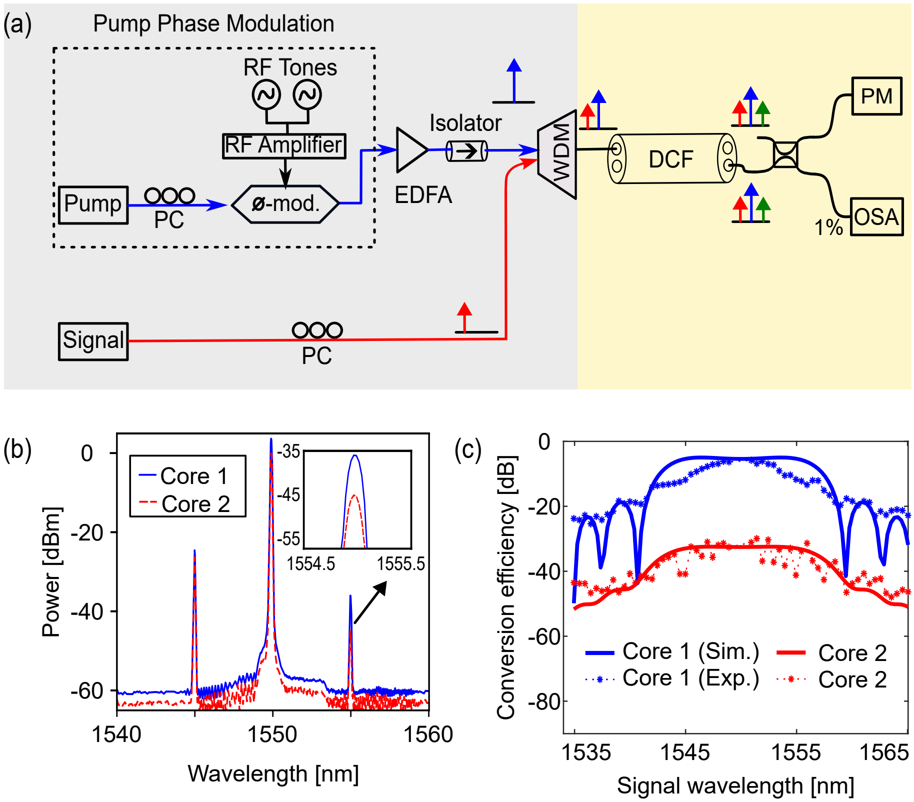

Figure 3.5: Schematic of the experimental setup for wavelength conversion in a coupled dual-core fiber, (b) the corresponding output spectrum showing idler generation, and (c) the measured conversion efficiency when both the pump and signal are launched into a single core.

conversion efficiency, the idler wavelength experiences different coupling strengths. As a result, fluctuations in the idler power give rise to variations in the conversion efficiency, as shown in Fig. 3.5(c). The reduction in the bandwidth of core 1 can be attributed to the PMD, and the fact that the zero-dispersion wavelength fluctuates along the fiber [100, 101]. The FWM spectrum is shown in figure 3.5(b).

3.3 Power-Dependent Mode Coupling

The nonlinear coherent coupler extends the conventional directional coupler by incorporating Kerr nonlinearity into the coupling dynamics [102].

It is based on the coherent interaction of two optical waveguides placed near each other. When low optical power is launched into one of the waveguides, the optical fields interact through the overlap of their evanescent fields, resulting in periodic power transfer between the two waveguides. In the nonlinear regime, as the input optical power increases, Kerr nonlinearity significantly modifies the power exchange dynamics between the waveguides. The resulting intensity-dependent refractive index induces nonlinear phase shifts that modify the propagation constants, thereby reducing the coupling efficiency and suppressing power transfer between the waveguides. As a result, optical power tends to remain confined within the launched waveguide [103]. These effects give rise to strong nonlinear transmission characteristics that can be exploited for all-optical switching, signal processing, and high-speed optical communication applications.

The response of a medium can be decomposed into perturbed and unperturbed polarization components. The unperturbed part corresponds to the linear response of a single isolated waveguide, while the perturbed part includes linear contributions from modal-field overlap with a neighboring waveguide and nonlinear contributions arising from the nonlinear response of the material, as described analytically in [102].

Mode coupling in the nonlinear regime is simulated using the coupled NLSEs presented in Section 3.2. For low input power, the coupled waveguides act as a conventional phase-matched coupler, where optical power switches from one core to another when $Cz = \pi/2$. Here, for a weakly coupled waveguide, the coupling strength C is taken as 4.5×10^{-4} m^{-1}, and z denotes the propagation length. The characteristic length $z = L_C$, at which light transfers back and forth between the two waveguides, is termed as coupling length. At critical power, the phase detuning induced in both waveguides becomes equal; consequently, there is no net detuning, and the power starts to remain trapped in the same waveguide. At high power, nonlinear effects modify the coupling length and reduce the amount of light coupled between the waveguides. At sufficiently high power, the detuning induced by the nonlinear refractive index becomes so large that it prevents a 50/50 power distribution, and phase matching is never achieved. As a result, most of the optical power remains confined to the input waveguide. The linear and nonlinear light propagation along the dual coupled-core fiber when one core is excited is shown in Figure 3.6(c).

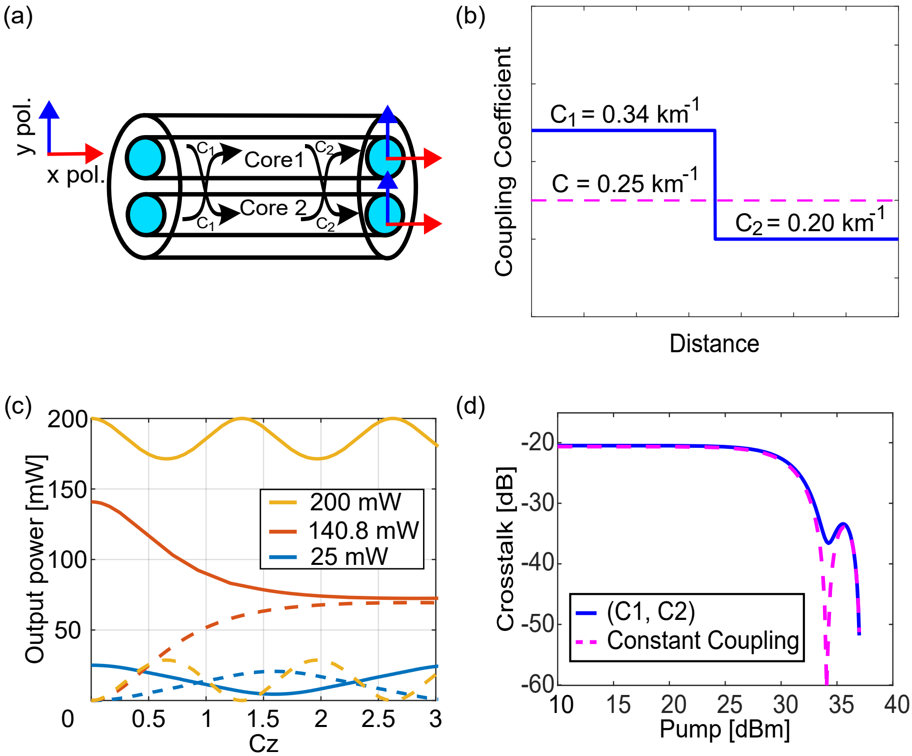

Figure 3.6: Schematic representation of (a) longitudinally varying coupling coefficients C_1 and C_2 in the first and second half of the dual-core fiber, and (b) their comparison with constant coupling coefficients. (c) Output of the coupled dual-core fiber showing the transition from the linear to the nonlinear regime, and (d) power-dependent crosstalk under two different coupling conditions.

The mode coupling in an ideal (unperturbed) MCF is described by a constant coupling coefficient between the modes. However, real MCFs have several perturbations, as discussed in Chapter 2, which can cause the coupling coefficients to vary along the propagation direction. To model the effect of longitudinally varying coupling strength on power suppression in coupled MCFs, we assume a coupling coefficient C_1 in the first half of the fiber and C_2 in the second half of the fiber, which is the simplest model for longitudinally varying coupling strength as shown in Fig. 3.6 (a). For an unperturbed fiber, the coupling coefficient C remains constant throughout the fiber length, as shown in Fig. 3.6(b). This accounts for longitudinal fluctuations in the coupling strength due to fabrication imperfections and random perturbations.

Efficient power transfer between cores occurs when the phase-matching condition is satisfied. As the optical power increases, nonlinear phase shifts modify the phase-matching condition, reducing the efficiency of inter-core power transfer. Consequently, a large fraction of the optical power remains confined within the launched core, resulting in suppression of power coupling to the adjacent core. At sufficiently high power levels, however, the interplay between the linear coupling and nonlinearity can break the phase-matching condition, leading to a change in the power-transfer dynamics. The constant coupling strength results in sharp inter-core crosstalk suppression. However, when longitudinal variations in the coupling strength are introduced along the fiber by considering two different coupling coefficients, $C_1 = 0.34$ km^{-1} and $C_2 = 0.20$ km^{-1}, the phase-matching condition is disrupted. This leads to an abrupt change in the inter-core crosstalk suppression behavior, as shown in Fig. 3.6(d). Phase matching can also be altered by the presence of random wavelength-dependent coupling variations along the fiber. Since crosstalk is highly sensitive to the coupling coefficients, discrepancies between idealized theoretical predictions and experimental measurements can be understood by a longitudinally varying coupling coefficient.

Experimental Implementation

The experimental setup for measuring power and polarization-dependent coupling is shown in Figure 3.7. The setup consists of a tunable laser and a high power EDFA with a maximum power output of about 2.5 W. At high optical powers, SBS limits system performance by reflecting a significant fraction of the total input optical power once the SBS threshold is reached. To mitigate SBS, the input laser is phase-modulated, as described in Section 3.1. The modulated signal is then amplified using an EDFA and passes through an isolator, which helps protect the optical components from damage by blocking back-scattered light from the DCF. Since crosstalk is polarization-dependent, as demonstrated in Paper [A], a polarization controller is used to align the state of polarization of the input signal before injecting to one of the cores of DCF. To measure nonlinear crosstalk, the input power is swept from 0 dBm to 30 dBm, and the output powers from both cores of the DCF are simultaneously measured using two power meters (PM).

The effect of polarization on nonlinear coupling is shown in Fig. 4 of Paper [A]. The experimental results show that varying the input state of

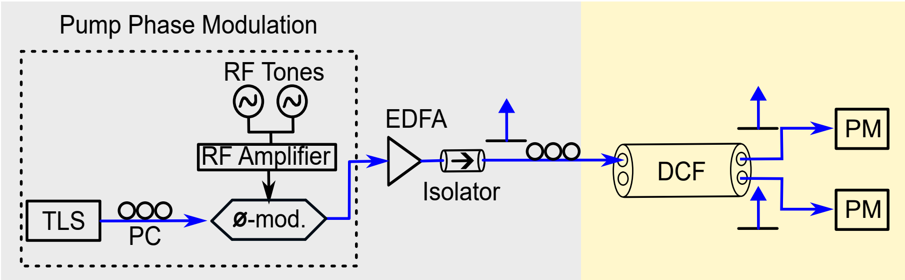

Figure 3.7: Schematic of the experimental setup for the measurement of power-dependent crosstalk in a dual-core fiber.

polarization of the launched signal causes significant changes in the linear crosstalk, as discussed in Paper [A]. The power-dependent coupling measurements are performed for two different input SOPs which corresponds to the minimum and maximum crosstalk in the linear regime. Different input SOPs exhibit different coupling behaviors in the coupled MCF due to variations in the effective coupling strength arising from randomly distributed perturbations along the fiber. Furthermore, even in an ideal MCF, the coupling strengths of the two orthogonal polarization states are not identical, giving rise to polarization-mode coupling, as discussed in detail in Paper [C].

In single-mode fibers, polarization mode dispersion and nonlinearity together influence the SOP of the propagating wave [104]. However, in coupled-core multi-core fibers, another interacting effect arises from linear coupling. In the nonlinear regime, as the pump power increases, the influence of PMD which primarily affects the input SOP corresponding to minimum crosstalk, diminishes due to the enhanced self-polarization effect of the pump. When the pump power exceeds a certain threshold, cross-polarization terms, which are sensitive to phase mismatch induced by birefringence, become comparatively negligible. Consequently, both SOPs converge toward the same crosstalk level.

3.4 Modal Dispersion-Induced FWM

Serena et al. [105] presented an ergodic Gaussian-noise (GN) model for strongly-coupled space-division multiplexed fibers, where optical channels evolve under the combined influence of Kerr nonlinearity, random mode coupling, and spatial modal dispersion (SMD). The optical fiber

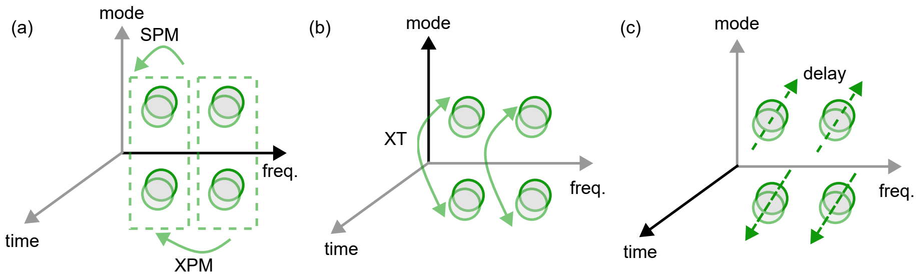

Figure 3.8: Schematic representation of the evolution of two optical frequency channels under (a) Kerr nonlinearity, (b) linear crosstalk (XT), and (c) SMD. Each circle denotes a channel localized in time, frequency, and mode space [105].

which supports multiple strongly-coupled spatial and polarization modes, signal propagation can be described by the multi-component Manakov equation, which accounts for fiber attenuation, chromatic dispersion, Kerr nonlinearity, mode coupling, and SMD. In the strong-coupling regime, modes continuously exchange energy due to random perturbations, while small differences in their group velocities introduce spatial modal dispersion. The transmitted WDM signal is represented as a collection of orthogonal channels distributed across time, frequency, spatial mode, and polarization dimensions. During propagation, these channels experience Kerr nonlinear interactions, linear crosstalk between modes, and SMD-induced temporal spreading, as illustrated in Fig.3.8.

In a coupled-core multi-core fiber, excitation of an individual core results in the optical field being distributed across all cores through inter-core coupling. When uncorrelated signals are transmitted through a coupled MCF, the averaging of nonlinear effects across coupled-cores leads to lower effective nonlinear impairments than in an equivalent SMF [106, 107]. Spatial modal dispersion is the temporal spread of an optical signal caused by differences in the group delays of the spatial modes, or supermodes, supported by a coupled MCF. It arises because frequency-dependent coupling leads to different propagation constants and group velocities for the supermodes, as discussed in Section 2.3.1. Small core-to-core variations in refractive index, together with bending, twisting, and temperature fluctuations, further modify the group delays. Consequently, signal components propagating in different spatial modes may arrive at the fiber output at different times [48, 108]. In coupled MCFs, SMD can be significantly larger than the PMD of conventional SMFs, depending on the fiber design and external perturbations.

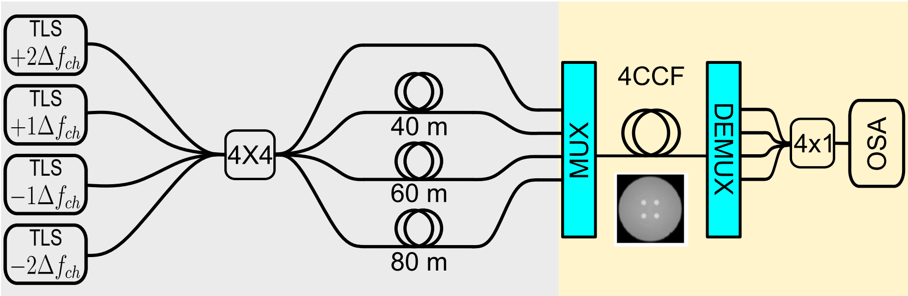

Figure 3.9: Schematic of the experimental setup for modal-dispersion-induced four-wave mixing.

3.4.1 Experimental Implementation

The randomly-coupled multi-core fiber used in this measurement is a 69.3 km four coupled-core fiber, which is field deployed in the city of L'Aquila, Italy [109, 110]. The SMF of 74.1 km is also deployed in the same tunnel together with the four coupled-core fiber. The propagation losses of the MCF and SMF are 0.227 and 0.246 dB/km, respectively, while their corresponding second-order dispersion parameters (β_2) are -24.4 ps^2/km and -21.7 ps^2/km, respectively [111].

Paper [D] discusses the impact of modal dispersion on FWM efficiency and estimates the nonlinear coefficient in a randomly-coupled multi-core fiber. The experimental setup used for the characterization of the nonlinear coefficient in a coupled-core multi-core fiber is shown in Fig. 3.9. The setup consists of four tunable lasers, each frequency-offset by Δf_{ch}. Using a 4×4 coupler, the outputs of the four continuous-wave (CW) laser tones are combined and split into four output port each carries an identical copy of the four CW tones. Before launching the signals into the coupled-core multi-core fiber, the tones in three of the branches are passed through delay arms of 40 m, 60 m, and 80 m, respectively, to decorrelate the signals injected into each core. The output of the coupled MCF is combined using a 4×1 coupler, and the resulting spectrum is recorded using an OSA. The measured spectral components are normalized to the average received peak power of the CW tones, such that the received power values are compensated for propagation loss and normalized relative to the input power. The total insertion loss, including the laser output coupling, patch cords, and fan-in/fan-out devices, is approximately 3 dB. For measurements using an SMF, only one output port of the 4×4 coupler is used to maintain approximately the same launch power per core as that used in the multi-core fiber measurements. The response of FWM is measured at 193 THz using four CW tones positioned at frequency offsets of $\pm 1\Delta f_{\mathrm{ch}}$ and $\pm 2\Delta f_{\mathrm{ch}}$ with respect to the channel under test.

3.4.2 Enhanced FWM by Modal Dispersion

In Paper [D], we experimentally demonstrated enhanced FWM efficiency induced by modal dispersion, together with a four-fold reduction in nonlinearity, in a field-deployed four coupled-core fiber. Paper [D] demonstrates that nonlinear effects in coupled-core multi-core fibers are governed not only by the material nonlinearity of the silica glass, but also by the spatial-mode dynamics created by inter-core coupling and modal dispersion. The experimental observation of a modal-dispersion-induced increase in four-wave-mixing efficiency shows that propagation differences between the guided supermodes can modify the phase-matching condition and enhance nonlinear frequency conversion. Consequently, modal dispersion should not be regarded only as a transmission impairment; it can also provide an additional design parameter for controlling nonlinear interactions in multi-core fibers. The presence of SMD enhances four-wave mixing efficiency in MCFs relative to the dispersionless condition [112], an effect well described by the ergodic GN model. The reduction in efficiency caused by core count is independent of the configuration, whereas the SDM-induced enhancement becomes dominant at large channel spacings.

Paper [D] also characterize the effective nonlinear coefficients of field deployed coupled MCF to evaluates its real performance. A lower effective nonlinear coefficient may reduce nonlinear transmission penalties and permit higher launch powers, whereas dispersion-assisted phase matching can selectively enhance four-wave mixing at particular wavelengths. This suggests that coupled-core multi-core fibers can be designed to suppress unwanted nonlinear distortion while improving nonlinear processes. The average nonlinear interaction across N-cores of a coupled MCF, arising from the dynamics of $2N$ spatial and polarization modes, is represented by $\kappa\bar{\gamma}$, where κ is a dimensionless parameter and $\bar{\gamma}$ is the effective nonlinear coefficient, which depend on the fiber parameters and modal structure. For a coupled MCF, $\bar{\gamma}$ and κ are given by [107]

$$\bar{\gamma} = \frac{2\pi f_0 n_2}{cNA_{\text{eff}}}, \quad \kappa = \frac{4}{3}\left(\frac{2N}{2N+1}\right), \tag{3.22}$$

where f_0 is the central frequency of the fundamental mode, n_2 is the Kerr nonlinear refractive index, and A_{eff} is the effective area of the core.

The findings presented in Paper [D] have important implications for the development of future space-division-multiplexed communication systems, in which multi-core fibers can increase transmission capacity by transmitting several spatial channels within a single cladding. They may also support applications such as wavelength and supermode conversion [113], parametric amplification, broadband light generation [114], and nonlinear optical signal processing [115]. More generally, the results show that the linear and nonlinear properties of coupled-core multicore fibers must be considered together when designing practical high-capacity SDM systems.

Chapter 4

Statistical Model for Random Mode Coupling

The nonlinear effects in coupled-core multi-core fibers were discussed in the previous chapter. In this chapter, a statistical model for random coupling is presented. The input–output relationship of a multi-core fiber can be described by its transfer matrix. In an ideal coupled MCF, the elements of the transfer matrix remain constant over time. However, due to fabrication imperfections and environmental perturbations, the transfer matrix elements fluctuate with time. These fluctuations lead to temporal variations in the optical power of the spatial and polarization modes, which are discussed in detail in this chapter. For a three coupled-core fiber, the coupled power can be represented on a two-dimensional simplex using a barycentric coordinate representation, as discussed in Paper [B]. In addition, a theoretical model is presented that describes the temporal drift of random mode coupling. Finally, the statistical properties of the coupled power fraction, including its probability density function and autocorrelation function, are analyzed.

4.1 Temporal Dynamics of Random Coupling

The spatial coupling, together with polarization-mode interactions, strongly influences system performance in the presence of birefringence, fabrication-induced asymmetries, and environmental perturbations. This section distinguishes the coupling dynamics of the spatial and polarization modes in the coupled MCF and investigates the temporal behavior of these random coupling fluctuations through experimental measurements.

4.1.1 Spatial and Polarization Mode Coupling

Spatial mode coupling refers to the transfer of optical power between different spatial channels (cores) as light propagates along a coupled-core multi-core fiber [116]. When light is launched into one core, coupling causes a fraction of the optical field to transfer to neighboring cores. The propagation of the optical fields is described by coupled-mode theory as discussed in chapter 2, where the field amplitude of each core also depends on the coupling from neighboring cores. The strength of interaction between cores is determined by the coupling coefficients. In an ideal coupled MCF, the power transfer is deterministic and periodic. However, in a real MCF, fabrication imperfections and environmental perturbations continuously modify the coupling coefficients. As a result, the optical power becomes randomly distributed among the cores over time, and the resulting output in one core is a mixture of the fields from all cores [48].

Each spatial mode (or core) supports two orthogonal polarization states. Polarization mode coupling is the transfer of optical power between orthogonal polarizations due to birefringence induced by fiber imperfections such as micro- and macro-bending, refractive index variations, core ellipticity, and core pitch variation along the fiber, as well as environmental perturbations caused by surrounding temperature variations, mechanical strain, and stress [117, 118]. Random variations in birefringence cause the state of polarization to vary continuously along the fiber and over time [119]. It can be intra-core or inter-core, depending on whether the orthogonal polarization states couple to each other within the same core or to neighboring cores. In a coupled N-core fiber, the total number of spatial modes is N and the number of polarization modes is $2N$. For the 4CCF, this gives eight modes, corresponding to two orthogonal polarization modes per core. The spatial and polarization coupling dynamics for a 4CCF are shown in Fig. 4.1.

In coupled-core multi-core fibers, both spatial and polarization mode coupling occur simultaneously. Therefore, the optical field is distributed among multiple cores as well as multiple polarization states. Over a sufficiently long time under strong coupling regime, the optical field evolves toward a statistical equilibrium in which all spatial and polarization modes become statistically equivalent. Understanding these dynamics is essential for the design and optimization of robust MCF-based polarization transmission and signal-processing systems.

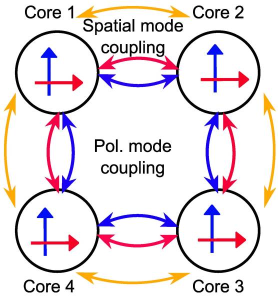

Figure 4.1: Coupling dynamics of spatial and polarization modes in coupled-core multi-core fibers.

Consider a symmetric N-coupled-core fiber in which power transfer among the cores can be modeled using a scalar model. The optical-field in the system is described by a complex transfer matrix $\mathbf{T}(\omega, t) \in \mathbb{C}^{N\times N}$, whose matrix elements are denoted by $m_{ij}(\omega, t)$. Assuming that the transfer matrix is unitary, it satisfies $\mathbf{T}^{\dagger}(\omega, t)\mathbf{T}(\omega, t) = \mathbf{I}$, which ensures that the total power is conserved. If only one of the core of coupled MCF is excited, the input field is $\mathbf{u}_{\text{in}} = u_0(1, 0, \ldots, 0)^T$, and the corresponding output field is

$$\mathbf{u}_{\text{out}}(\omega, t) = \mathbf{T}(\omega, t)\mathbf{u}_{\text{in}} = u_0 \begin{pmatrix} m_{11}(\omega, t) \\ m_{21}(\omega, t) \\ \vdots \\ m_{N1}(\omega, t) \end{pmatrix}. \tag{4.1}$$

The total output power is defined as the squared Euclidean norm of the output field,

$$P_{\text{tot}}(t) = \|\mathbf{u}_{\text{out}}(\omega, t)\|^2 = \mathbf{u}_{\text{out}}^{\dagger}\mathbf{u}_{\text{out}}. \tag{4.2}$$

Substituting Eq. (4.1) into Eq. (4.2) gives

$$\begin{aligned} P_{\text{tot}}(t) &= |u_0|^2 \left(m_{11}^* \; m_{21}^* \; \cdots \; m_{N1}^*\right) \begin{pmatrix} m_{11} \\ m_{21} \\ \vdots \\ m_{N1} \end{pmatrix} \\ &= |u_0|^2 \sum_{i=1}^{N} |m_{i1}(\omega, t)|^2 = |u_0|^2, \end{aligned} \tag{4.3}$$

where the last equality follows from the unitarity of the transfer matrix, which implies that each column of $\mathbf{T}$ has unit norm. More generally, for an arbitrary input field

$$\mathbf{u}_{\text{in}} = \begin{pmatrix} u_1^{\text{in}} \\ u_2^{\text{in}} \\ \vdots \\ u_N^{\text{in}} \end{pmatrix},$$

the output field is

$$\mathbf{u}_{\text{out}}(\omega, t) = \mathbf{T}(\omega, t)\mathbf{u}_{\text{in}},$$

whose ith component is

$$u_i^{\text{out}}(\omega, t) = \sum_{j=1}^{N} m_{ij}(\omega, t) u_j^{\text{in}}.$$

Therefore, the optical power at the output of core i is

$$P_i(t) = \left| \sum_{j=1}^{N} m_{ij}(\omega, t) u_j^{\text{in}} \right|^2. \tag{4.4}$$

The total output power can be written as

$$\begin{aligned} P_{\text{tot}}(t) &= \sum_{i=1}^{N} P_i(t) \\ &= \mathbf{u}_{\text{in}}^{\dagger} \mathbf{T}^{\dagger}(\omega, t)\mathbf{T}(\omega, t)\mathbf{u}_{\text{in}} \\ &= \mathbf{u}_{\text{in}}^{\dagger}\mathbf{u}_{\text{in}}, \end{aligned} \tag{4.5}$$

The temporal evolution of the transfer matrix elements $m_{ij}(\omega, t)$ manifests as temporal fluctuations in the output power distribution among the coupled-cores. Therefore, by continuously monitoring the output power of each core, the temporal drift of the transfer matrix and hence the coupling dynamics of the coupled MCF can be experimentally characterized.

4.1.2 Experimental Implementation

To measure the temporal drift of the coupled power induced by different types of external and internal perturbations in the coupled MCF, as discussed in Section 2.3.2. The experimental setups for measuring the temporal drift of spatial mode and polarization mode coupling are shown in Fig. 4.2(a) and Fig. 4.2(b), respectively. Paper [B] discusses only the

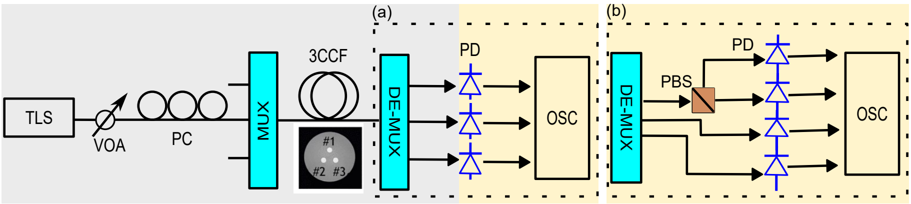

Figure 4.2: Schematic of the experimental setup for measuring the temporal fluctuations of (a) spatially coupled optical power and (b) orthogonal polarization modes over time in a strongly-coupled three-core fiber.

spatial mode coupling dynamics in a three coupled-core fiber, whereas Paper [C] investigates both the spatial mode coupling dynamics and the polarization mode coupling dynamics in a four coupled-core fiber.

The experimental setup consists of a tunable laser source (TLS) operating in the C-band. A variable optical attenuator (VOA) is used to adjust the optical power for the measurement in the linear regime. The output of the VOA is connected to a polarization controller (PC), which is used to optimize the input state of polarization such that the output power is maximized across all coupled spatial modes when the optical signal is launched into one of the cores of the coupled MCF. Two different detection schemes were used to monitor the temporal drift of spatial mode and polarization mode coupling, as shown in Fig. 4.2(a) and Fig. 4.2(b), respectively. At the output of the coupled fiber, the optical power is distributed among the coupled spatial modes rather than remaining entirely in the launched core. The output power distribution depends on the propagation length and the coupling strength between the coupled cores. Therefore, for the three coupled-core fiber (3CCF), three identical photo-detectors were used to simultaneously monitor the temporal fluctuations of the optical power in the individual cores. The outputs of the photo-detectors were connected to a real-time oscilloscope to record the optical power over time.

For the measurement of the temporal drift of polarization mode coupling, the output from one of the cores is separated into two orthogonal polarization components, namely the x- and y-polarization states, using a polarization beam splitter (PBS). As shown in Fig. 4.2(b), the two polarization components are detected simultaneously using two identical photodetectors. The optical power from the remaining cores is also monitored to ensure that the total output power remains constant during the measurement. The corresponding electrical signals from all photodetec-

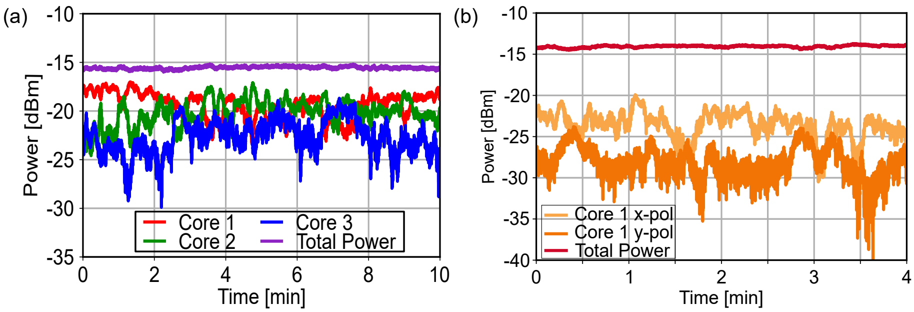

Figure 4.3: Instantaneously measured temporal evolution of (a) the coupled fractional power and (b) the orthogonal polarization-mode power, together with the total output power, in a strongly-coupled three-core fiber.

tors are recorded using a real-time oscilloscope to monitor the temporal fluctuations of the polarization mode coupling.

The temporal evolution of the fractional coupled power in each core of the three-coupled-core fiber, together with the total output power, is shown in Fig. 4.3(a). The temporal variations of the x- and y-polarization components of core 1, along with the total output power, are shown in Fig. 4.3(b). When light is launched into one of the cores of the coupled-core multi-core fiber, the optical field is redistributed among all the coupled cores through the transfer matrix $\mathbf{T}(\omega, t)$. For a single-core excitation, the output field is determined by the first column of the transfer matrix, whose elements $m_{i1}(\omega, t)$ represent the complex coupling coefficients from the excited input core to the (i)th output core. In the absence of loss, the transfer matrix is unitary, ensuring that the total optical power is conserved, i.e., the sum of the output powers in all cores remains equal to the input power.

Fabrication imperfections and environmental fluctuations continuously perturb the propagation constants and coupling characteristics of the coupled-core fiber. As a result, the transfer matrix elements $m_{ij}(\omega, t)$ become time dependent. Although the total output power remains constant due to the unitarity of the transfer matrix, the magnitudes and phases of the individual transfer matrix elements fluctuate with time, causing a redistribution of optical power among the output cores. Consequently, the fractional power measured at each core exhibits temporal drift, which directly reflects the temporal fluctuations of the transfer matrix.

4.2 Time-varying Random Coupling Model

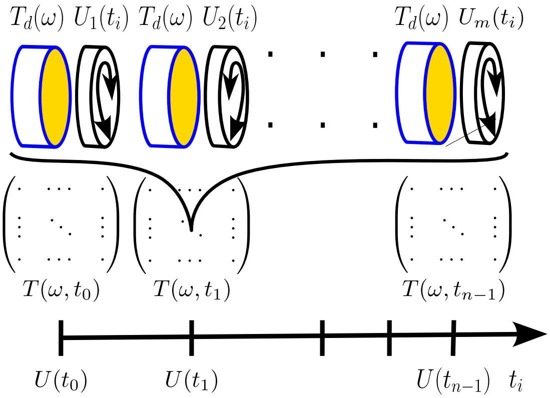

Figure 4.4: Concatenated wave-plate model for time-varying transfer matrix for random coupling in coupled-core multi-core fibers.

As shown above, the coupling characteristics of a coupled-core multi-core fiber are not constant over time. In practice, the fiber is continuously subjected to various perturbations that modify the effective propagation constants and coupling coefficients of the guided modes, resulting in temporal variations in the transfer matrix that describes the fiber.

The random coupling in a coupled MCF can be modeled using the concatenated waveplate model, which originates from the PMD formalism [72, 120]. In this, the fiber is divided into m short segments with $m = 1, 2, \ldots, N$. Each segment, of length L_d, represents the propagation interval over which the coupling characteristics remain approximately constant. Between two successive segments, a random unitary matrix, $U_m(t_i)$ is introduced to model the effect of environmental perturbations such as temperature fluctuation, acoustic vibrations, and mechanical stress. Unlike the static random coupling model, where a single random unitary matrix $\mathbf{U}_m$ is used for each fiber concatenation, the dynamic random coupling model uses a time-varying unitary matrix $\mathbf{U}_m(t)$ for each fiber concatenation as done in [121]. The total transfer function is obtained by cascading the transfer matrices of all fiber segments as shown in Fig. 4.4. The instantaneous random unitary matrix at each time is given by

$$\mathbf{U}(t_{i+1}) = \Delta\mathbf{U}_i \, \mathbf{U}(t_i), \tag{4.6}$$

Here, each matrix $\mathbf{U}(t_i)$ corresponds to the i^{th} time instance, where $i = 0, 1, 2, \ldots, n-1$. The discrete time points n are uniformly separated by the time interval δt. The change in the unitary matrix between two consecutive time instants, $\mathbf{U}(t_i)$ and $\mathbf{U}(t_{i+1})$, is represented by an incremental unitary matrix $\Delta\mathbf{U}_i$, which accounts for weak environmental perturbations during each time interval and is given by

$$\Delta\mathbf{U}_i = \exp\left(j\gamma\mathbf{H}_i\right), \tag{4.7}$$

where $\gamma \ll 1$ is a dimensionless parameter that determines the strength of the fluctuations and controls the temporal correlation between two consecutive unitary matrices, $\mathbf{U}(t_i)$ and $\mathbf{U}(t_{i+1})$. Smaller values of γ correspond to weaker environmental fluctuations and, consequently, longer temporal correlations. Larger values of γ result in stronger fluctuations and faster temporal decorrelation. The random Hermitian matrix $\mathbf{H}_i = \mathbf{H}_i^\dagger$ is independently chosen from the Gaussian Unitary Ensemble with expectation values $\langle\mathbf{H}_i\rangle = 0$ and $\langle\mathbf{H}_i^2\rangle = D\mathbf{I}$, which ensures that all states are statistically equally likely over the unitary group. Here D denotes the dimension of the transfer matrix and $\mathbf{I}$ is the identity matrix. The Hermitian property ensures that $\Delta\mathbf{U}_i$ remains unitary, thereby preserving the total optical power. Following the approach presented in [121], the total transfer matrix shows that temporal fluctuations results from the cumulative effect of many independent, weak perturbations. Under the assumption of strong mode mixing and statistical isotropy, the transfer matrix of the coupled MCF can be modeled as a random unitary matrix [122] and the real and imaginary parts of the transfer matrix elements can be approximated by Gaussian random variables with zero mean. The real and imaginary parts of the first element, m_{11} of the transfer matrix, along with their corresponding probability density functions, are shown in Fig. 4.5(a) and (b), respectively.

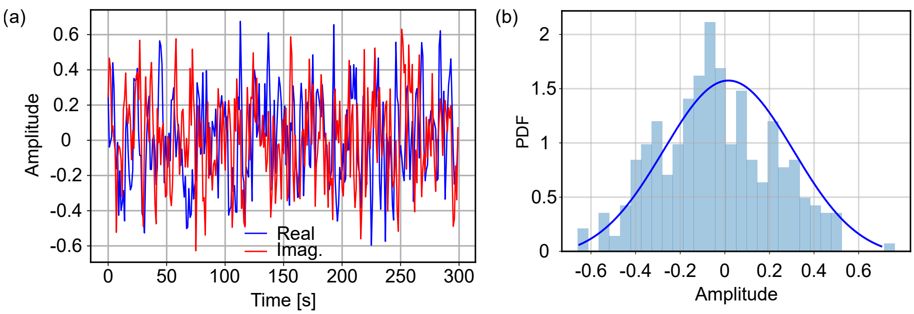

Figure 4.5: (a) Real and imaginary components of the first transfer matrix element, m_{11} and (b) its probability density function.

4.3 Probability and Correlation Functions

As discussed in paper [B], in a three coupled-core fiber the optical power is continuously redistributed among the three cores in a random manner through random mode coupling. However, the powers in individual cores remain correlated because only a fraction of the total power is transferred to each core. By introducing the normalized power fractions as $p_i = P_i(t)/P_{tot}$, the constraint $p_1 + p_2 + p_3 = 1$ is satisfied. Since the total optical power remains constant over time, the state of the system is uniquely determined by the triplet (p_1, p_2, p_3). Consequently, the normalized power fractions are not independent; only two degrees of freedom remain, with the third variable being uniquely determined by the other two. The normalized fractional power (p_1, p_2, p_3) can be mapped onto a two-dimensional simplex (triangle) using barycentric coordinates [123]. This representation provides a convenient geometric way to represent the power sharing among the three cores. It gives an intuitive visualization of the stochastic evolution of the coupled fractional power, as described in more detail in Paper [B].

With the concatenated fiber model described in Section 4.2, random perturbations in coupled MCF are represented by a random unitary matrix inserted between successive fiber sections to model stochastic random mode coupling. The elements of the unitary matrix is described by Haar distribution [124], which ensures power conservation and statistically isotropic mode mixing. Since the transfer matrix is unitary, the squared magnitudes of the elements in each row are non-negative random variables whose sum is unity. Consequently, these vectors are confined to a simplex and can be naturally described by a multivariate Dirichlet distribution [125]. Therefore, the normalized power fractions (p_1, p_2, p_3) follow a Dirichlet distribution. The marginal distribution of each component of the Dirichlet distribution is a Beta distribution [126]. Consequently, the normalized optical power in each core follows a Beta distribution, which is discussed below.

4.3.1 Symmetric Dirichlet Distribution

Consider a strongly-coupled three-core fiber in which the cores are symmetrically arranged at the vertices of an equilateral triangle. When optical power is launched into one of the cores, strong coupling causes the power to be continuously redistributed among all three cores during propagation. The normalized power fractions satisfy $\sum_{i=1}^{3} p_i = 1$ with

$p_i \geq 0$, where p_i denotes the fractional power in the ith core. Assuming statistical symmetry among the three cores, their joint probability density function (PDF) can be modeled using a symmetric Dirichlet distribution as [127]

$$f(p_1, p_2, p_3) = C(\alpha) p_1^{\alpha-1} p_2^{\alpha-1} p_3^{\alpha-1}, \tag{4.8}$$

where $\alpha > 0$ is a free parameter and $C(\alpha)$ is the normalization constant which ensures the total PDF integrates to unity. Since the total power is constant, one of the fractional powers can always be eliminated; e.g., $p_3 = 1 - p_1 - p_2$. The joint PDF can then be expressed in terms of the two independent variables as

$$f(p_1, p_2) = C(\alpha) p_1^{\alpha-1} p_2^{\alpha-1} (1 - p_1 - p_2)^{\alpha-1}. \tag{4.9}$$

To determine the probability density of the fractional power in one core, the joint PDF is integrated over the remaining variable,

$$f(p_1) = \int_0^{1-p_1} f(p_1, p_2)\, dp_2. \tag{4.10}$$

Substituting Eq. (4.9) into Eq. (4.10) gives

$$f(p_1) = C(\alpha) p_1^{\alpha-1} \int_0^{1-p_1} p_2^{\alpha-1} (1 - p_1 - p_2)^{\alpha-1}\, dp_2. \tag{4.11}$$

The integral can be simplified further using the substitution $p_2 = x(1 - p_1)$, which transforms the integration limits from $p_2 \in [0, 1 - p_1]$ to $x \in [0, 1]$. The Equation (4.11) becomes

$$f(p_1) = C(\alpha) p_1^{\alpha-1} (1 - p_1)^{2\alpha-1} \int_0^1 x^{\alpha-1} (1 - x)^{\alpha-1} dx. \tag{4.12}$$

Comparing the above integral with the Beta function,

$$B(a, b) = \int_0^1 x^{a-1} (1 - x)^{b-1} dx, \tag{4.13}$$

which gives

$$f(p_1) = C(\alpha) B(\alpha, \alpha) p_1^{\alpha-1} (1 - p_1)^{2\alpha-1}. \tag{4.14}$$

The normalization constant $C(\alpha)$ is obtained from the condition

$$\int_0^1 f(p_1)\, dp_1 = 1,$$

which gives

$$C(\alpha) = \frac{1}{B(\alpha,\alpha)B(\alpha,2\alpha)}. \tag{4.15}$$

Using the Gamma-function identity of the Beta function,

$$B(a,b) = \frac{\Gamma(a)\Gamma(b)}{\Gamma(a+b)}, \tag{4.16}$$

the normalization constant simplifies to

$$C(\alpha) = \frac{\Gamma(3\alpha)}{\Gamma(\alpha)^3}. \tag{4.17}$$

Substituting Eq. (4.17) into Eq. (4.14) finally gives the marginal distribution

$$f(p_1) = \frac{\Gamma(3\alpha)}{\Gamma(\alpha)\Gamma(2\alpha)} p_1^{\alpha-1}(1-p_1)^{2\alpha-1}. \tag{4.18}$$

Therefore, the marginal distribution of each component of a symmetric three-dimensional Dirichlet distribution follows a Beta distribution. From the symmetry of the Dirichlet distribution, the same result also holds for p_2 and p_3. Consequently, each individual core power fraction is Beta distributed, while the joint distribution of the three power fractions is governed by the symmetric Dirichlet distribution. For a symmetric Dirichlet distribution, the marginal distribution of each normalized fractional power p_i is characterized by a single free parameter α. The corresponding mean and variance are given by [128]

$$\mathbb{E}[p_i] = \frac{1}{3}, \quad \mathrm{Var}(p_i) = \frac{2}{9(3\alpha+1)}. \tag{4.19}$$

As the parameter α increases, the probability density function becomes progressively narrower and more sharply peaked around its mean. Consequently, the spread of the distribution decreases with increasing values of α, indicating that the normalized power fractions become increasingly concentrated around their mean value, as shown in Figs. 4.6(a) and 4.6(b). The parameter α controls the spread and uniformity of the distribution. Physically, it is related to the variance (spread) of the normalized power fractions. To illustrate the effect of α on the power distribution among the coupled cores, let us consider two cases with $\alpha = 2$ and $\alpha = 6$. As shown in Fig. 4.6(c), the distribution is relatively broad, with the probability density spread over a large region of the simplex, whereas Fig. 4.6(d) shows that, as α increases, the distribution

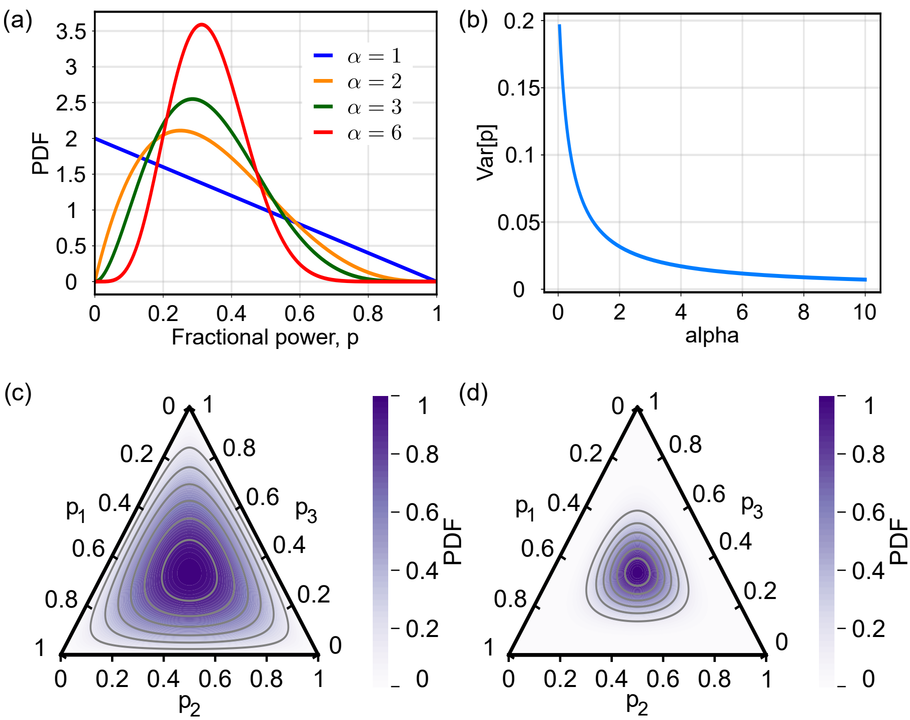

Figure 4.6: (a) Probability density function of the Beta distribution and (b) the corresponding variance as a function of parameter α. (c) Examples of the simplex representation of the Dirichlet distribution for $\alpha = 2$ and (d) $\alpha = 6$.

becomes increasingly concentrated and shrinks toward the center of the simplex. The case $\alpha = 1$ corresponds to a uniform distribution over the simplex, whereas larger values of α leads to more peaked distributions around the mean. In this sense, α governs the statistical distribution of power among the three cores by controlling the magnitude of fluctuations in the normalized power fractions. In Fig. 4.7(a), we can see that, over the short time period ($\sim$5 hours), the measured PDF of the y polarization is slightly shifted relative to that of the x polarization, whereas in Fig. 4.7(b), over the longer duration ($\sim$50 hours), both PDFs converge toward symmetric distributions. The asymmetric distribution of polarization mode coupling is nontrivial in the sense that we expect both polarization modes to couple identically in the coupled MCF, but experimentally it was observed that the PDF of the temporal variation is an asymmetric distribution for short times of measurement. In an ideal MCF, the two orthogonal polarization modes are expected to

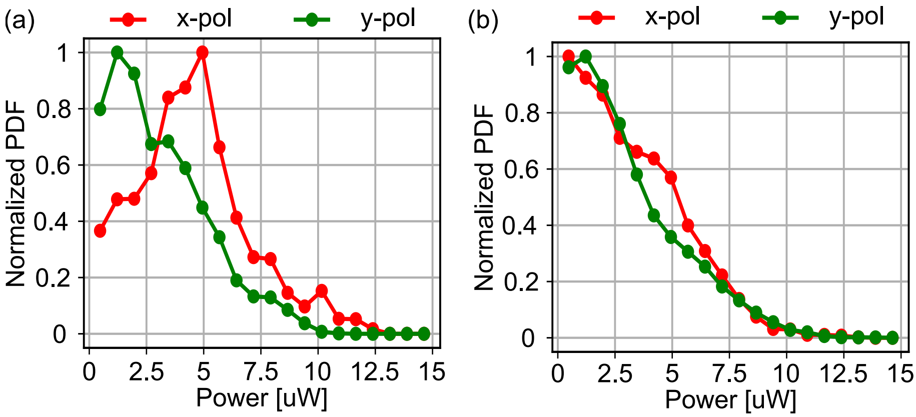

Figure 4.7: The measured probability distribution functions of the two orthogonal polarization modes, (x-pol and y-pol) in the 4-CCF for a short time interval ($\sim$ 5 hours) and (b) a longer period ($\sim$ 50 hours).

couple identically. However, in a real MCF, perturbation-induced birefringence breaks the symmetry of the fiber. As a result, over short time intervals, the coupled-core multi-core fiber exhibits a bias toward one polarization mode over the other. A possible explanation is that, during the fabrication of the coupled-core multi-core fiber, residual mechanical stresses may be introduced in a non-uniform manner across the fiber cross-section and along its length. These stress inhomogeneities can induce local birefringence variations in each core, thereby modifying the polarization propagation constants and the coupling behavior between the orthogonal polarization modes. As a result, the polarization-mode coupling may no longer remain fully symmetric, which can give rise to the observed asymmetry in the polarization-mode statistics. Another reason is that, over a short time period, the Jones vector is not isotropically distributed over a $2N$-dimensional hyper-sphere, since the state of polarization does not have sufficient time to explore all possible polarization states. As a result, one polarization component may exhibit a biased behavior relative to the other.

The asymmetry in the probability distribution function of the polarization modes can also be reflected in the total probability distribution function of the spatial modes over short time intervals, where the parameter α characterizes the degree of asymmetry. A general model extending the Dirichlet distribution to account for this behavior is still under investigation and is left for future work.

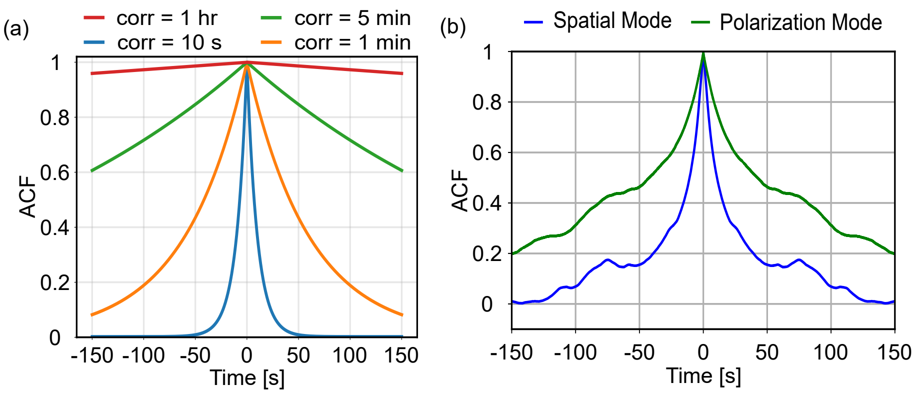

Figure 4.8: (a) Analytical autocorrelation functions for spatial modes with different correlation time and (b) measured autocorrelation functions for both the spatial and polarization modes of the 3CCF.

4.3.2 Autocorrelation function

The correlation coefficient between two random variables X and Y, with expectation values μ_X and μ_Y and standard deviations σ_X and σ_Y, respectively, is defined as [129]

$$\mathrm{corr}(X, Y) = \frac{E[(X - \mu_X)(Y - \mu_Y)]}{\sigma_X \sigma_Y}. \tag{4.20}$$

Here, $E[\cdot]$ denotes the expectation operator, and $\mathrm{corr}(X, Y)$ represents the correlation coefficient between X and Y. In the case of autocorrelation, the two random variables correspond to two realizations of the same stochastic process evaluated at different time instants, i.e., $X = X(t)$ and $Y = X(t')$. The autocorrelation function therefore quantifies the correlation between the signal values at times t and t', and is given by [130]

$$R_{tt'} = \frac{E[(X(t) - \mu_X)(X(t') - \mu_X)]}{\sigma_X^2}. \tag{4.21}$$

The autocorrelation function (ACF) measures the correlation of a signal with a time-shifted version of itself. It quantifies the similarity of the signal at two different time instants separated by a time lag. The analytical expression for the autocorrelation function of the random power fluctuations of the spatial modes is given by [121]

$$R_{tt'} = \exp\left(-\frac{|t - t'|}{\tau_{corr}}\right) \tag{4.22}$$

where τ_{corr} denotes the correlation time of the signal, defined as the time lag at which the normalized autocorrelation decreases to $1/e$ of its maximum value. The equation shows that the temporal corelation caused by perturbations between the signal at two different time decays exponentially with increasing time lag $|t-t'|$, attains its maxima at $t=t'$, where the signal is perfectly correlated with itself. Physically, the correlation time τ_{corr} represents the characteristic time scale over which causes the system to decorrelate. In other words, A smaller value of τ_{corr} indicates rapid channel variations and faster decorrelation due to stronger or more rapidly environmental drifts. whereas, a large value of τ_{corr} implies a more slow decorrelation which the system remains correlated over longer time intervals as shown in Fig. 4.8 (a). Therefore, the correlation time provides a quantitative measure of the temporal stability of the coupled-core multi-core fiber and is an important parameter for characterizing the dynamic behavior of the channel under realistic conditions.

The ACF of the spatial modes is found to decorrelate faster than that of the polarization modes in the three coupled-core fiber, as shown in Fig. 4.8(b). A model for the autocorrelation of the polarization modes is still under investigation and is left for future work.

Chapter 5

Summary and Future Outlook

This thesis focuses on the linear and nonlinear characterization of coupling dynamics in coupled-core multi-core fibers [131,132]. The interplay between linear coupling and Kerr nonlinearity has a significant impact on the performance of SDM systems [133], and there is a need to understand the coupling dynamics in coupled-core multi-core fibers for the robust design of SDM transmission systems [134, 135] and SDM-based photonic devices. The results presented in this work open many follow-up questions and several directions for future research that need to be addressed. We discuss some of the most relevant research gaps highlighted by this work.

Paper [A] investigates wavelength and polarization-dependent coupling, as well as the effect of coupling strength on parametric interactions such as wavelength conversion in weakly-coupled dual-core fibers. The results showed that the nonlinear response depends sensitively on the longitudinally varying coupling in a real (perturbed) coupled-MCF. The extension of this work is therefore to study the effect of coupling on the parametric gain spectrum. As theoretically demonstrated in [136,137] for parametric amplification in dual-core fibers, coupling can compensate for chromatic dispersion [138] and lead to a flat gain spectrum. Extending the analysis of Paper [A] in this direction could provide valuable insight into the role of random coupling on the gain characteristics of optical parametric amplifiers (OPAs) based on coupled-core multi-core fibers.

Paper [B] investigates the statistical properties of time-varying spatial-mode coupling in a randomly-coupled three-core fiber. In the linear regime, the probability distribution function of the fractional coupled power follow a symmetric Dirichlet distribution [139, 140] characterized by a single free parameter, α. An interesting direction for future research is to investigate the impact of pump power on the parameter α in the non-linear regime. As shown in Paper [A], at high optical power, non-linear suppression of optical power happens in coupled-cores which causes the optical power to remain localized within the same core. Therefore, it would also be interesting to study the strength of the temporal fluctuations and characterize their statistical properties in the nonlinear regime.

Paper [C] investigates the statistical characteristics of spatial and polarization-mode coupling in a randomly-coupled four-core fiber. The results show that, for short-time measurements, the fiber does not exhibit isotropic behavior, and the probability distribution functions of the two orthogonal polarization modes are asymmetric. However, for long-term measurements, the fiber tends toward isotropic behavior, and the PDFs gradually converge to a symmetric distribution. There is a need to develop a unified statistical model [141] that can capture the short-term and long-term behavior of the fiber in a single model. Such a model would provide a more complete description of the spatial and polarization coupling dynamics across all time scales. Furthermore, to our knowledge, there have been limited theoretical and experimental studies on the statistical distribution of spatial and polarization-mode coupling in randomly coupled MCFs operating in the non-linear regime [142], which provides an opportunity to extend the work of Paper [B] and [C].

Apart from coupled-core multi-core fibers, another promising direction is the study of coupling dynamics in hollow-core optical fibers [143], where light propagation occurs predominantly in air rather than silica [144]. With reduced non-nonlinearities, low latency [145–147], and distinct sensitivity to environmental perturbations, hollow-core fibers provide a fundamentally different propagation medium compared to conventional solid-core fibers. Investigating spatial and polarization coupling in such structures may offer new insight into the role of birefringence, perturbation-induced mode mixing, and temporal stability in next-generation fiber-based transmission and signal-processing systems.

Finally, the concepts implemented in this thesis may also be extended beyond coupled MCFs to integrated photonic devices. One of the main limitations of coupled-core multi-core fibers is that the coupling strength is determined by the core pitch and fiber geometry during fabrication, which gives limited flexibility for design optimization. In contrast, integrated photonic platforms offer substantially greater freedom in dispersion engineering, waveguide separation, coupling length, and device geometry, which provides more control to tune coupling dynamics. This gives an opportunity to use the concepts of coupling studied in coupled-core multi-core fibers to integrated photonic circuits. In particular, a promising research direction is to exploit the dynamics of non-linear coupling to demonstrate the all-optical switching in coupled spirals on silicon nitride platforms [148, 149]. Such devices could find important applications in all-optical signal processing, optical communication systems, high-speed photonic interconnects for data centers and quantum photonic computing.

Chapter 6

Summary of Papers

Paper A

Investigation of Nonlinear Coupling and Parametric Interactions in Coupled Multi-Core Fibers,
European Conference on Optical Communications (ECOC), IEEE, 2025.

In this paper, we experimentally investigated the linear and nonlinear coupling characteristics of a coupled MCF showing that the nonlinear response of a perturbed coupled MCF is highly sensitive to longitudinal coupling variations. At high power, most of the optical power remains in the same core, suppressing inter-core power transfer. The paper also studied the effect of coupling on wavelength conversion efficiency.

Contributions: I performed the measurements and simulations, wrote the paper with support from the co-authors, and presented the work at ECOC 2025.

Paper B

Statistical analysis of the temporal dynamics of coupling in strongly coupled multi-core fibers,
Optics Express, 34, 25321–25333, 2026.

The paper is devoted for the characterization of the temporal dynamics of coupling in a strongly-coupled multi-core fiber. It shows that the statistical distribution of the fractional coupled power follows a beta distribution, which is a marginal distribution of the Dirichlet distribution.

Contributions: I performed the measurements and simulations, wrote the paper with support from the co-authors.

Paper C

Statistical Characterization of Spatial and Polarization Mode Coupling in Field-Deployed Coupled-core Multi-core Fibers,
European Conference on Optical Communications (ECOC), 2026.

The paper describes the time behavior of the four-core coupled-core fiber. It shows that the fiber at short time is not isotropic and the distribution tends to be asymmetric, whereas with sufficiently long time, the isotropy is restored. The polarization modes are shown to decorrelate faster than the spatial modes, which explains the two different time scale of coupling dynamics in these types of fiber.

Contributions: I performed the measurements and simulations, wrote the paper with support from the co-authors.

Paper D

Experimental Observation of Modal-Dispersion-Induced FWM Efficiency Increase and Non-linearity Coefficient Characterization in Deployed Coupled-Core Multi-Core Fibers,
European Conference on Optical Communications (ECOC), 2026.

The paper is devoted to the experimental study of effect of modal dispersion on four-wave mixing in a field-deployed randomly coupled multi-core fiber. It shows that the FWM efficiency is enhanced by the presence of spatial mode dispersion. The nonlinear coefficient is also measured experimentally, showing a four-fold reduction in the effective nonlinearity of the randomly-coupled multi-core fiber compared with the co-deployed standard single-mode fiber.

Contributions: I assisted the author with the experimental measurements.

References

[1] A. Rao, A. Legout, Y.-s. Lim, D. Towsley, C. Barakat, and W. Dabbous, "Network characteristics of video streaming traffic," in *Proceedings of the Seventh Conference on Emerging Networking EXperiments and Technologies*, ser. CoNEXT '11. New York, NY, USA: Association for Computing Machinery, 2011.

[2] G. Keiser, "Fiber optic communication networks," in *Fiber Optic Communications.* Springer, 2021, pp. 507–575.

[3] R.-J. Essiambre, G. Kramer, P. J. Winzer, G. J. Foschini, and B. Goebel, "Capacity limits of optical fiber networks," *Journal of Lightwave Technology*, vol. 28, no. 4, pp. 662–701, 2010.

[4] K. C. Kao and G. A. Hockham, "Dielectric-fibre surface waveguides for optical frequencies," in *Proceedings of the Institution of Electrical Engineers*, vol. 113, no. 7. IET, 1966, pp. 1151–1158.

[5] F. P. Kapron, D. B. Keck, and R. D. Maurer, "Radiation losses in glass optical waveguides," *Applied Physics Letters*, vol. 17, no. 10, pp. 423–425, 1970.

[6] K. Fujiwara, G. Tanaka, and S. Kurosaki, "Method of manufacturing glass for optical waveguide," US Patent 4,135,901, 1979.

[7] S. Shiraishi, K. Fujiwara, and S. Kurosaki, "An optical transmission fiber containing fluorine," US Patent 4,082,420, 1978.

[8] J. MacChesney, "Preparation of low loss optical fibers using simultaneous vapor phase deposition and fusion," *Xth Int. Congr. Glass*, vol. 6, p. 40, 1974.

[9] R. J. Mears, L. Reekie, I. Jauncey, and D. N. Payne, "Low-noise erbium-doped fibre amplifier operating at 1.54 μm," *Electronics letters*, vol. 23, no. 19, pp. 1026–1028, 1987.

[10] G. P. Agrawal, *Fiber-optic communication systems.* John Wiley & Sons, 2012.

[11] I. Sector, "ITU-T Recommendation G. 694.1: Spectral grids for WDM applications: DWDM frequency grid," 2002.

[12] R.-J. Essiambre, G. Kramer, P. J. Winzer, G. J. Foschini, and B. Goebel, "Capacity limits of optical fiber networks," *Journal of Lightwave technology*, vol. 28, no. 4, pp. 662–701, 2010.

[13] D. J. Richardson, J. M. Fini, and L. E. Nelson, "Space-division multiplexing in optical fibres," *Nature photonics*, vol. 7, no. 5, pp. 354–362, 2013.

[14] P. J. Winzer and R.-J. Essiambre, "Advanced optical modulation formats," in *Optical Fiber Telecommunications VB.* Elsevier, 2008, pp. 23–93.

[15] K. Kikuchi, "Fundamentals of coherent optical fiber communications," *Journal of lightwave technology*, vol. 34, no. 1, pp. 157–179, 2015.

[16] D.-S. Ly-Gagnon, S. Tsukamoto, K. Katoh, and K. Kikuchi, "Coherent detection of optical quadrature phase-shift keying signals with carrier phase estimation," *J. Lightwave Technol.*, vol. 24, no. 1, p. 12, 2006.

[17] T. Pfau, S. Hoffmann, and R. Noe, "Hardware-efficient coherent digital receiver concept with feedforward carrier recovery for M-QAM constellations," *Journal of Lightwave Technology*, vol. 27, no. 8, pp. 989–999, 2009.

[18] P. P. Mitra and J. B. Stark, "Nonlinear limits to the information capacity of optical fibre communications," *Nature*, vol. 411, no. 6841, pp. 1027–1030, 2001.

[19] C. E. Shannon, "Communication in the presence of noise," *Proceedings of the IRE*, vol. 37, no. 1, pp. 10–21, 1949.

[20] T. Mizuno and Y. Miyamoto, "High-capacity dense space division multiplexing transmission," *Optical Fiber Technology*, vol. 35, pp. 108–117, 2017.

[21] W. Shi, Y. Tian, and A. Gervais, "Scaling capacity of fiber-optic transmission systems via silicon photonics," *Nanophotonics*, vol. 9, no. 16, pp. 4629–4663, 2020.

[22] S. Inao, "High density multi-core-fiber cable," in *Proc. of the 28th International Wire & Cable Symposium (IWCS), 1979*, 1979, pp. 370–384.

[23] L. NOANE, "Ultra high density cables using a new concept of bunched multicore monomode fibers: A key for the future ftth networks," in *Proc. Int. Wire & Cables Symp., Nov. 1994*, 1994, pp. 203–210.

[24] B. J. Puttnam, R. S. Luis, G. Rademacher, Y. Awaji, and H. Furukawa, "1 Pb/s transmission in a 125μm diameter 4-core MCF," in *CLEO: Science and Innovations.* Optica Publishing Group, 2022, pp. JTh6B–1.

[25] D. Soma, Y. Wakayama, S. Beppu, S. Sumita, T. Tsuritani, T. Hayashi, T. Nagashima, M. Suzuki, M. Yoshida, K. Kasai, M. Nakazawa, H. Takahashi, K. Igarashi, I. Morita, and M. Suzuki, "10.16-Peta-B/s Dense SDM/WDM Transmission Over 6-Mode 19-Core Fiber Across the C+L Band," *Journal of Lightwave Technology*, vol. 36, no. 6, pp. 1362–1368, 2018.

[26] T. Sakamoto, T. Matsui, T. Yamamoto, K. Tsujikawa, and K. Nakajima, "Recent progress of multi-core fiber technologies," in *Asia Communications and Photonics Conference.* Optica Publishing Group, 2017, p. M1J.1.

[27] K. Takenaga, S. Tanigawa, N. Guan, S. Matsuo, K. Saitoh, and M. Koshiba, "Reduction of crosstalk by quasi-homogeneous solid multi-core fiber," in *Optical Fiber Communication Conference.* Optica Publishing Group, 2010, p. OWK7.

[28] M. Nakazawa, M. Yoshida, and T. Hirooka, "Nondestructive measurement of mode couplings along a multi-core fiber using a synchronous multi-channel OTDR," *Optics express*, vol. 20, no. 11, pp. 12 530–12 540, 2012.

[29] Y. Kobayashi, T. Suganuma, T. Hayashi, T. Hasegawa, M. Yoshida, and M. Nakazawa, "Characterization of inter-core

crosstalk of multi-core fiber as a function of bending radius with multi-channel OTDR," in *2022 27th OptoElectronics and Communications Conference (OECC) and 2022 International Conference on Photonics in Switching and Computing (PSC)*. IEEE, 2022, pp. 1–3.

[30] S. O. Arik, J. M. Kahn, and K.-P. Ho, "MIMO signal processing for mode-division multiplexing: An overview of channel models and signal processing architectures," *IEEE Signal Processing Magazine*, vol. 31, no. 2, pp. 25–34, 2014.

[31] R. Ryf, S. Randel, A. H. Gnauck, C. Bolle, A. Sierra, S. Mumtaz, M. Esmaeelpour, E. C. Burrows, R.-J. Essiambre, P. J. Winzer *et al.*, "Mode-division multiplexing over 96 km of few-mode fiber using coherent 6× 6 MIMO processing," *Journal of Lightwave technology*, vol. 30, no. 4, pp. 521–531, 2012.

[32] K.-P. Ho and J. M. Kahn, "Mode-dependent loss and gain: statistics and effect on mode-division multiplexing," *Optics express*, vol. 19, no. 17, pp. 16 612–16 635, 2011.

[33] N. K. Fontaine, R. Ryf, M. A. Mestre, B. Guan, X. Palou, S. Randel, Y. Sun, L. Grüner-Nielsen, R. V. Jensen, and R. Lingle, "Characterization of space-division multiplexing systems using a swept-wavelength interferometer," in *2013 Optical Fiber Communication Conference and Exposition and the National Fiber Optic Engineers Conference (OFC/NFOEC)*. IEEE, 2013, pp. 1–3.

[34] N. K. Fontaine, "Characterization of space-division multiplexing fibers using swept-wavelength interferometry," in *2015 Optical Fiber Communications Conference and Exhibition (OFC)*. IEEE, 2015, pp. 1–3.

[35] K. Twayana, Z. Ye, Ó. B. Helgason, K. Vijayan, M. Karlsson, and V. Torres-Company, "Frequency-comb-calibrated swept-wavelength interferometry," *Optics Express*, vol. 29, no. 15, pp. 24 363–24 372, 2021.

[36] E. D. Moore, "Advances in swept-wavelength interferometry for precision measurements," Ph.D. dissertation, University of Colorado at Boulder, 2011.

[37] E. Deriushkina, I. Rebolledo-Salgado, M. Mazur, V. Torres-Company, P. Andrekson, J. Schroeder, and M. Karlsson, "Dual-comb swept-wavelength interferometry: Theory and experiment," *Journal of Lightwave Technology*, vol. 40, no. 19, pp. 6508–6516, 2022.

[38] M. Mazur, N. K. Fontaine, M. Karlsson, P. A. Andrekson, J. Schröder *et al.*, "Dual-comb swept wavelength interferometry," in *CLEO: Applications and Technology.* Optica Publishing Group, 2020, pp. JW2B–23.

[39] B. Kalla, M. Cappelletti, M. van den Hout, V. van van Vliet, S. Rommel, L. Palmieri, T. Bradley, and C. Okonkwo, "Approaches for mitigating polarization-induced fading in optical vector network analyzer for long-length SDM fiber characterization," *Journal of Lightwave Technology*, vol. 43, no. 13, pp. 6161–6167, 2025.

[40] M. Ohashi, Y. Miyoshi, H. Kubota, R. Maruyama, and N. Kuwaki, "Longitudinal fiber parameter measurements of multi-core fiber using OTDR," *Optics Express*, vol. 22, no. 24, pp. 30 137–30 147, 2014.

[41] J. Xiong, L. Ma, Y. Chang, T. Cheng, L. Shen, L. Zhang, C. Yan, L. Sun, Q. Liu, and Z. He, "Study on characteristics of coupled-core four-core fibers with different core pitches," *IEEE Photonics Journal*, vol. 16, no. 1, pp. 1–7, 2023.

[42] R.-J. Essiambre and R. W. Tkach, "Capacity trends and limits of optical communication networks," *Proceedings of the IEEE*, vol. 100, no. 5, pp. 1035–1055, 2012.

[43] P. Winzer, *Spatial Multiplexing: The Next Frontier in Network Capacity Scaling*, pp. 372–374.

[44] B. J. Puttnam, R. S. Luís, G. Rademacher, A. Alfredsson, W. Klaus, J. Sakaguchi, Y. Awaji, E. Agrell, and N. Wada, "Characteristics of homogeneous multi-core fibers for SDM transmission," *APL photonics*, vol. 4, no. 2, 2019.

[45] T. Hayashi and T. Nakanishi, "Multi-core optical fibers for the next-generation communications," *SEI Tech. Rev.*, vol. 86, pp. 23–28, 2018.

[46] T. Mizuno, H. Takara, A. Sano, and Y. Miyamoto, "Dense space-division multiplexed transmission systems using multi-core and multi-mode fiber," *Journal of lightwave technology*, vol. 34, no. 2, pp. 582–592, 2015.

[47] T. Hayashi, T. Taru, O. Shimakawa, T. Sasaki, and E. Sasaoka, "Design and fabrication of ultra-low crosstalk and low-loss multi-core fiber," *Opt. Express*, vol. 19, no. 17, pp. 16 576–16 592, 2011.

[48] K. Saitoh, "Multi-core fiber technology for SDM: Coupling mechanisms and design," *Journal of Lightwave Technology*, vol. 40, no. 5, pp. 1527–1543, 2022.

[49] T. Hayashi, T. Sasaki, and E. Sasaoka, "Multi-core fibers for high capacity transmission," in *OFC/NFOEC*, 2012, pp. 1–3.

[50] K. Abedin, T. Taunay, M. Fishteyn, M. Yan, B. Zhu, J. Fini, E. Monberg, F. Dimarcello, and P. Wisk, "Amplification and noise properties of an erbium-doped multicore fiber amplifier," *Optics express*, vol. 19, no. 17, pp. 16 715–16 721, 2011.

[51] K. Abedin, T. Taunay, M. Fishteyn, D. DiGiovanni, V. Supradeepa, J. Fini, M. Yan, B. Zhu, E. Monberg, and F. Dimarcello, "Cladding-pumped erbium-doped multicore fiber amplifier," *Optics express*, vol. 20, no. 18, pp. 20 191–20 200, 2012.

[52] C. Jin, B. Ung, Y. Messaddeq, and S. LaRochelle, "Annular-cladding erbium doped multicore fiber for SDM amplification," *Optics express*, vol. 23, no. 23, pp. 29 647–29 659, 2015.

[53] Y. Tsuchida, K. Maeda, Y. Mimura, H. Matsuura, R. Miyabe, K. Aiso, and R. Sugizaki, "Amplification characteristics of a multi-core erbium-doped fiber amplifier," in *OFC/NFOEC*. IEEE, 2012, pp. 1–3.

[54] P. M. Krummrich, "Optical amplification and optical filter based signal processing for cost and energy efficient spatial multiplexing," *Optics express*, vol. 19, no. 17, pp. 16 636–16 652, 2011.

[55] T. Hayashi, T. Sakamoto, Y. Yamada, R. Ryf, R.-J. Essiambre, N. Fontaine, M. Mazur, H. Chen, and T. Hasegawa, "Randomly-coupled multi-core fiber technology," *Proceedings of the IEEE*, vol. 110, no. 11, pp. 1786–1803, 2022.

[56] B. E. Saleh and M. C. Teich, *Fundamentals of photonics, 2 volume set.* john Wiley & sons, 2019.

[57] K.-P. Ho, J. M. Kahn, I. Kaminow, T. Li, and A. Willner, “Mode coupling and its impact on spatially multiplexed systems,” *Optical Fiber Telecommunications VI*, vol. 17, pp. 1386–1392, 2013.

[58] A. M. Ortiz and R. L. Sáez, “Multi-core optical fibers: Theory, applications and opportunities,” *Sel. Top. Opt. Fiber Technol. Appl*, vol. 2, pp. 63–102, 2018.

[59] L. Palmieri, “Mode coupling in optical fibers,” *Journal of Lightwave Technology*, 2025.

[60] A. W. Snyder, “Coupled-mode theory for optical fibers,” *Journal of the optical society of America*, vol. 62, no. 11, pp. 1267–1277, 1972.

[61] C. Xia, M. A. Eftekhar, R. A. Correa, J. E. Antonio-Lopez, A. Schülzgen, D. Christodoulides, and G. Li, “Supermodes in coupled multi-core waveguide structures,” *IEEE Journal of Selected Topics in Quantum Electronics*, vol. 22, no. 2, pp. 196–207, 2015.

[62] C. Xia, N. Bai, I. Ozdur, X. Zhou, and G. Li, “Supermodes for optical transmission,” *Optics express*, vol. 19, no. 17, pp. 16 653–16 664, 2011.

[63] C. Xia, N. Bai, R. Amezcua-Correa, E. Antonio-Lopez, A. Schulzgen, M. Richardson, X. Zhou, and G. Li, “Supermodes in strongly-coupled multi-core fibers,” in *2013 Optical Fiber Communication Conference and Exposition and the National Fiber Optic Engineers Conference (OFC/NFOEC).* IEEE, 2013, pp. 1–3.

[64] T. Zhao, W. Ren, T. Yin, and F. Wang, “Calculation of the coupling coefficient of twin-core fiber based on the supermode theory with finite element method,” *Optics and Photonics Journal*, vol. 11, no. 8, pp. 402–411, 2021.

[65] I. H. Malitson, “Interspecimen comparison of the refractive index of fused silica,” *Journal of the optical society of America*, vol. 55, no. 10, pp. 1205–1209, 1965.

[66] M. Cappelletti, M. Mazur, N. K. Fontaine, R. Ryf, T. Hayashi, A. Mecozzi, M. Santagiustina, A. Galtarossa, C. Antonelli, and L. Palmieri, “Statistical analysis of modal dispersion in field-installed coupled-core fiber link,” *Journal of Lightwave Technology*, vol. 42, no. 11, pp. 4103–4109, 2024.

[67] H. Bissessur, A. Busson, and F. Hedaraly, “Impact of inter-core crosstalk in unrepeatered transmission over 2-core MCF,” *Journal of Lightwave Technology*, 2026.

[68] G. Rademacher, R. S. Luís, B. J. Puttnam, Y. Awaji, and N. Wada, “Crosstalk dynamics in multi-core fibers,” *Optics express*, vol. 25, no. 10, pp. 12 020–12 028, 2017.

[69] T. Hayashi, T. Taru, O. Shimakawa, T. Sasaki, and E. Sasaoka, “Characterization of crosstalk in ultra-low-crosstalk multi-core fiber,” *Journal of Lightwave Technology*, vol. 30, no. 4, pp. 583–589, 2011.

[70] T. Hayashi, T. Taru, O. Shimakawa, T. Sasaki, and E. Sasaoka, “Uncoupled multi-core fiber enhancing signal-to-noise ratio,” *Optics express*, vol. 20, no. 26, pp. B94–B103, 2012.

[71] R. Imada, T. Sakamoto, T. Sato, K. Saitoh, and K. Nakajima, “Group delay spread calculation based on individual core-mode-based supermode analysis for randomly coupled multi-core fiber,” *Journal of Lightwave Technology*, 2026.

[72] K.-P. Ho and J. M. Kahn, “Statistics of group delays in multimode fiber with strong mode coupling,” *Journal of lightwave technology*, vol. 29, no. 21, pp. 3119–3128, 2011.

[73] R. M. Kingsta and R. S. Selvakumari, “A review on coupled and uncoupled multicore fibers for future ultra-high capacity optical communication,” *Optik*, vol. 199, p. 163341, 2019.

[74] C. Lasagni, P. Serena, A. Bononi, A. Mecozzi, and C. Antonelli, “Investigation of mode-dependent loss in coupled-core multi-core fiber transmissions with fiber nonlinearities,” in *ECOC 2024; 50th European Conference on Optical Communication*. VDE, 2024, pp. 333–336.

[75] T. Hasegawa and T. Hayashi, "Measurement of mode dependent loss of randomly-coupled multi-core fiber using scrambling method," in *Optoelectronics and Communications Conference*. Optica Publishing Group, 2021, pp. T2C–2.

[76] R. Chiao, C. H. Townes, and B. Stoicheff, "Stimulated Brillouin scattering and coherent generation of intense hypersonic waves," *Physical review letters*, vol. 12, no. 21, p. 592, 1964.

[77] A. Kobyakov, M. Sauer, and D. Chowdhury, "Stimulated Brillouin scattering in optical fibers," *Advances in optics and photonics*, vol. 2, no. 1, pp. 1–59, 2009.

[78] A. Kobyakov, S. Kumar, D. Q. Chowdhury, A. B. Ruffin, M. Sauer, S. R. Bickham, and R. Mishra, "Design concept for optical fibers with enhanced SBS threshold," *Optics Express*, vol. 13, no. 14, pp. 5338–5346, 2005.

[79] A. Yeniay, J.-M. Delavaux, and J. Toulouse, "Spontaneous and stimulated Brillouin scattering gain spectra in optical fibers," *Journal of lightwave technology*, vol. 20, no. 8, p. 1425, 2002.

[80] G. Agrawal, *Nonlinear fiber optics*. Elsevier, 2012.

[81] J. Coles, *Advanced phase modulation techniques for stimulated Brillouin scattering suppression in fiber optic parametric amplifiers*. University of California, San Diego, 2009.

[82] R. U. Weerasuriya, R. Larsson, and P. A. Andrekson, "Effect of counter-phase pump modulation of phase-sensitive amplifiers noise performance and SBS suppression," *Optics Express*, vol. 33, no. 7, pp. 16 174–16 186, 2025.

[83] G. Stegeman, E. Wright, N. Finlayson, R. Zanoni, and C. Seaton, "Third order nonlinear integrated optics," *Journal of Lightwave Technology*, vol. 6, no. 6, pp. 953–970, 1988.

[84] M. Rumi and J. W. Perry, "Two-photon absorption: An overview of measurements and principles," *Advances in Optics and Photonics*, vol. 2, no. 4, pp. 451–518, 2010.

[85] V. Mizrahi, K. W. DeLong, G. I. Stegeman, M. A. Saifi, and M. J. Andrejco, "Two-photon absorption as a limitation to all-optical switching," *Opt. Lett.*, vol. 14, no. 20, pp. 1140–1142, 1989.

[86] P. S. Banks, M. D. Feit, and M. D. Perry, "High-intensity third-harmonic generation," *J. Opt. Soc. Am. B*, vol. 19, no. 1, pp. 102–118, 2002.

[87] T. Y. F. Tsang, "Optical third-harmonic generation at interfaces," *Phys. Rev. A*, vol. 52, pp. 4116–4125, 1995.

[88] D. N. Christodoulides, I. C. Khoo, G. J. Salamo, G. I. Stegeman, and E. W. V. Stryland, "Nonlinear refraction and absorption: mechanisms and magnitudes," *Adv. Opt. Photon.*, vol. 2, no. 1, pp. 60–200, 2010.

[89] R. W. Boyd, *Nonlinear Optics*, 4th ed. Academic Press, 2020.

[90] R. H. Stolen and J. E. Bjorkholm, "Parametric amplification and frequency conversion in optical fibers," *IEEE Journal of Quantum Electronics*, vol. 18, no. 7, pp. 1062–1072, 1982.

[91] Z. Tong, C. Lundström, P. A. Andrekson, M. Karlsson, and A. Bogris, "Ultralow noise, broadband phase-sensitive optical amplifiers, and their applications," *IEEE Journal of Selected Topics in Quantum Electronics*, vol. 18, no. 2, pp. 1016–1032, 2012.

[92] S. L. Olsson, H. Eliasson, E. Astra, M. Karlsson, and P. A. Andrekson, "Long-haul optical transmission link using low-noise phase-sensitive amplifiers," *Nature communications*, vol. 9, no. 1, p. 2513, 2018.

[93] Z. Tong, C. Lundström, P. Andrekson, C. McKinstrie, M. Karlsson, D. Blessing, E. Tipsuwannakul, B. Puttnam, H. Toda, and L. Grüner-Nielsen, "Towards ultrasensitive optical links enabled by low-noise phase-sensitive amplifiers," *Nature photonics*, vol. 5, no. 7, pp. 430–436, 2011.

[94] G. P. Agrawal, *Nonlinear Fiber Optics*, 6th ed. Academic Press, 2019.

[95] O. Aso, M. Tadakuma, and S. Namiki, "Four-wave mixing in optical fibers and its applications," *dEp*, vol. 1, no. 2, 1999.

[96] P. A. Andrekson and M. Karlsson, "Fiber-based phase-sensitive optical amplifiers and their applications," *Advances in Optics and Photonics*, vol. 12, no. 2, pp. 367–428, 2020.

[97] J. Hansryd, P. A. Andrekson, M. Westlund, J. Li, and P.-O. Hedekvist, “Fiber-based optical parametric amplifiers and their applications,” *IEEE Journal of Selected Topics in Quantum Electronics*, vol. 8, no. 3, pp. 506–520, 2002.

[98] V. Ribeiro, Á. D. Szabó, A. M. Rocha, C. B. Gaur, A. A. Ali, Y. Quiquempois, A. Mussot, G. Bouwmans, and N. Doran, “Parametric amplification and wavelength conversion in dual-core highly nonlinear fibers,” *Journal of Lightwave Technology*, vol. 40, no. 17, pp. 6013–6020, 2022.

[99] B.-S. Kim, Y. Chung, and S.-H. Kim, “Split-step time-domain analysis of optical waveguide devices composed of a directional coupler and gratings,” *Optics Letters*, vol. 25, no. 8, pp. 530–532, 2000.

[100] C. J. McKinstrie and M. Karlsson, “Effects of polarization-mode dispersion on degenerate four-wave mixing,” *Journal of Lightwave Technology*, vol. 35, no. 19, pp. 4210–4218, 2017.

[101] V. Ribeiro, M. Shi, and A. M. Perego, “Impact of zero-dispersion wavelength fluctuations in a coupled dual-core fiber optical parametric amplifier,” *Journal of Lightwave Technology*, vol. 41, no. 19, pp. 6235–6243, 2023.

[102] S. Jensen, “The nonlinear coherent coupler,” *IEEE Journal of Quantum Electronics*, vol. 18, no. 10, pp. 1580–1583, 1982.

[103] A. W. Snyder, D. Mitchell, L. Poladian, D. R. Rowland, and Y. Chen, “Physics of nonlinear fiber couplers,” *Journal of the Optical Society of America B*, vol. 8, no. 10, pp. 2102–2118, 1991.

[104] C. R. Menyuk and B. S. Marks, “Interaction of polarization mode dispersion and nonlinearity in optical fiber transmission systems,” *Journal of Lightwave Technology*, vol. 24, no. 7, p. 2806, 2006.

[105] P. Serena, C. Lasagni, A. Bononi, C. Antonelli, and A. Mecozzi, “The ergodic GN model for space-division multiplexing with strong mode coupling,” *Journal of Lightwave Technology*, vol. 40, no. 10, pp. 3263–3276, 2022.

[106] R. Ryf, N. K. Fontaine, S. H. Chang, J. C. Alvarado, B. Huang, J. Antonio-López, H. Chen, R.-J. Essiambre, E. Burrows, R. W. Tkach *et al.*, “Long-haul transmission over multi-core fibers with

coupled cores," in *2017 European Conference on Optical Communication (ECOC)*. IEEE, 2017, pp. 1–3.

[107] C. Antonelli, M. Shtaif, and A. Mecozzi, "Modeling of nonlinear propagation in space-division multiplexed fiber-optic transmission," *Journal of Lightwave Technology*, vol. 34, no. 1, pp. 36–54, 2015.

[108] C. Antonelli, A. Mecozzi, and M. Shtaif, "The delay spread in fibers for SDM transmission: Dependence on fiber parameters and perturbations," *Optics Express*, vol. 23, no. 3, pp. 2196–2202, 2015.

[109] R. Ryf, A. Marotta, M. Mazur, N. K. Fontaine, H. Chen, T. Hayashi, T. Nagashima, T. Nakanishi, T. Morishima, F. Graziosi *et al.*, "Transmission over randomly-coupled 4-core fiber in field-deployed multi-core fiber cable," in *2020 European Conference on Optical Communications (ECOC)*. IEEE, 2020, pp. 1–4.

[110] M. Mazur, N. K. Fontaine, R. Ryf, A. Marotta, H. Chen, T. Hayashi, T. Nagashima, T. Nakanishi, T. Morishima, F. Graziosi *et al.*, "Transfer matrix characterization of field-deployed MCFs," in *2020 European Conference on Optical Communications (ECOC)*. IEEE, 2020, pp. 1–4.

[111] T. Hayashi, T. Nagashima, T. Nakanishi, T. Morishima, R. Kawawada, A. Mecozzi, and C. Antonelli, "Field-deployed multi-core fiber testbed," in *2019 24th OptoElectronics and Communications Conference (OECC) and 2019 International Conference on Photonics in Switching and Computing (PSC)*. IEEE, 2019, pp. 1–3.

[112] C. Lasagni, P. Serena, A. Bononi, A. Mecozzi, and C. Antonelli, "On the impact of four-wave mixing in coupled-core multicore fiber transmissions," in *Optical Fiber Communication Conference*. Optica Publishing Group, 2025, pp. M1H–3.

[113] T. Hellwig, J. P. Epping, M. Schnack, K.-J. Boller, and C. Fallnich, "Ultrafast, low-power, all-optical switching via birefringent phase-matched transverse mode conversion in integrated waveguides," *Opt. Express*, vol. 23, no. 15, pp. 19 189–19 201, 2015.

[114] T. Sylvestre, E. Genier, A. N. Ghosh, P. Bowen, G. Genty, J. Troles, A. Mussot, A. C. Peacock, M. Klimczak, A. M. Heidt,

J. C. Travers, O. Bang, and J. M. Dudley, “Recent advances in supercontinuum generation in specialty optical fibers,” *J. Opt. Soc. Am. B*, vol. 38, no. 12, pp. F90–F103, 2021.

[115] S. M. Hendrickson, A. C. Foster, R. M. Camacho, and B. D. Clader, “Integrated nonlinear photonics: emerging applications and ongoing challenges,” *J. Opt. Soc. Am. B*, vol. 31, no. 12, pp. 3193–3203, 2014.

[116] L. Palmieri, “Mode coupling in optical fibers,” in *Optical Fiber Communication Conference (OFC) 2024*. Optica Publishing Group, 2024, p. M2A.5.

[117] C. Antonelli, G. Riccardi, T. Hayashi, and A. Mecozzi, “Role of polarization-mode coupling in the crosstalk between cores of weakly-coupled multi-core fibers,” *Optics Express*, vol. 28, no. 9, pp. 12 847–12 861, 2020.

[118] A. Macho, C. García-Meca, F. J. Fraile-Peláez, M. Morant, and R. Llorente, “Birefringence effects in multi-core fiber: coupled local-mode theory,” *Optics Express*, vol. 24, no. 19, pp. 21 415–21 434, 2016.

[119] M. Karlsson, J. Brentel, and P. A. Andrekson, “Long-term measurement of PMD and polarization drift in installed fibers,” *Journal of Lightwave Technology*, vol. 18, no. 7, pp. 941–951, 2000.

[120] G. Foschini and C. Poole, “Statistical theory of polarization dispersion in single mode fibers,” *Journal of Lightwave Technology*, vol. 9, no. 11, pp. 1439–1456, 1991.

[121] E. Deriushkina, J. Schröder, and M. Karlsson, “Dynamic model for coupled-core fibers,” *Journal of Lightwave Technology*, vol. 42, no. 23, pp. 8366–8373, 2024.

[122] A. Edelman and N. R. Rao, “Random matrix theory,” *Acta numerica*, vol. 14, pp. 233–297, 2005.

[123] M. S. Floater, “Generalized barycentric coordinates and applications,” *Acta Numerica*, vol. 24, pp. 161–214, 2015.

[124] N. J. Higham, *Accuracy and stability of numerical algorithms*. SIAM, 2002.

[125] B. A. Frigyik, A. Kapila, and M. R. Gupta, "Introduction to the dirichlet distribution and related processes," *Department of Electrical Engineering, University of Washignton, UWEETR-2010-0006*, vol. 6, pp. 1–27, 2010.

[126] S. Kotz, N. Balakrishnan, and N. L. Johnson, *Continuous multivariate distributions, Volume 1: Models and applications.* John wiley & sons, 2019, vol. 1.

[127] W. Feller, *An introduction to probability theory and its applications, Volume 2.* John Wiley & Sons, 1991, vol. 2.

[128] W. H. Beyer, "CRC standard mathematical tables and formulae," *Boca Raton*, 1991.

[129] M. Mazur, T. Taunay, T. Geisler, L. Gruener-Nielsen, M. Karlsson, and P. A. Andrekson, "Measurement of temperature-induced polarization drift and correlation in a 7-core fiber," in *ECOC 2016; 42nd European Conference on Optical Communication.* VDE, 2016, pp. 1–3.

[130] S. U. Pillai, *Probability, random variables, and stochastic processes.* McGraw-Hill, 2002.

[131] M. Raj, V. Ribeiro, G. Bouwmans, Y. Quiquempois, A. Mussot, P. Andrekson, and M. Karlsson, "Investigation of nonlinear coupling and parametric interactions in coupled multi-core fibers," in *2025 European Conference on Optical Communications (ECOC).* IEEE, 2025, pp. 1–4.

[132] M. Raj, T. Hayashi, P. Andrekson, and M. Karlsson, "Statistical analysis of the temporal dynamics of coupling in strongly coupled multi-core fibers," *Optics Express*, vol. 34, no. 14, pp. 25 321–25 333, 2026.

[133] G. P. Agrawal, S. Mumtaz, and R.-J. Essiambre, "Nonlinear performance of SDM systems designed with multimode or multicore fibers," in *Optical Fiber Communication Conference.* Optica Publishing Group, 2013, pp. OM3I–6.

[134] F. Y. Chan, A. P. T. Lau, and H.-Y. Tam, "Mode coupling dynamics and communication strategies for multi-core fiber systems," *Optics Express*, vol. 20, no. 4, pp. 4548–4563, 2012.

[135] W. Ren and Z. Tan, "A study on the coupling coefficients for multi-core fibers," *Optik*, vol. 127, no. 6, pp. 3248–3252, 2016.

[136] V. Ribeiro, M. Karlsson, and P. Andrekson, "Parametric amplification with a dual-core fiber," *Optics Express*, vol. 25, no. 6, pp. 6234–6243, 2017.

[137] V. Ribeiro, A. Lorences-Riesgo, P. Andrekson, and M. Karlsson, "Noise in phase-(in) sensitive dual-core fiber parametric amplification," *Optics Express*, vol. 26, no. 4, pp. 4050–4059, 2018.

[138] M. Shi, V. Ribeiro, and A. M. Perego, "Parametric amplification in coupled nonlinear waveguides: the role of coupling dispersion," *Frontiers in Photonics*, vol. 4, p. 1051294, 2023.

[139] K. W. Ng, G.-L. Tian, and M.-L. Tang, "Dirichlet and related distributions: Theory, methods and applications," 2011.

[140] I. J. Good, "On the application of symmetric dirichlet distributions and their mixtures to contingency tables," *The Annals of Statistics*, pp. 1159–1189, 1976.

[141] A. Macho, M. Morant, and R. Llorente, "Unified model of linear and nonlinear crosstalk in multi-core fiber," *Journal of Lightwave Technology*, vol. 34, no. 13, pp. 3035–3046, 2016.

[142] A. Macho, M. Morant, and R. Llorente, "Experimental evaluation of nonlinear crosstalk in multi-core fiber," *Optics Express*, vol. 23, no. 14, pp. 18 712–18 720, 2015.

[143] M. Komanec, D. Dousek, D. Suslov, and S. Zvanovec, "Hollow-core optical fibers," *Radioengineering*, vol. 29, pp. 417–430, 2020.

[144] E. N. Fokoua, S. A. Mousavi, G. T. Jasion, D. J. Richardson, and F. Poletti, "Loss in hollow-core optical fibers: mechanisms, scaling rules, and limits," *Adv. Opt. Photon.*, vol. 15, no. 1, pp. 1–85, 2023.

[145] B. Zhu, B. J. Mangan, T. Kremp, G. S. Puc, V. Mikhailov, K. Dube, Y. Dulashko, M. Cortes, Y. lian, K. Marceau, B. Violette, D. Cartsounis, R. Lago, B. Savran, D. Inniss, and D. J. DiGiovanni, "First demonstration of hollow-core-fiber cable for low latency data transmission," in *Optical Fiber Communication Conference Postdeadline Papers 2020.* Optica Publishing Group, 2020, p. Th4B.3.

[146] M. Kuschnerov, B. J. Mangan, K. Gong, V. A. J. M. Sleiffer, M. Herrmann, J. W. Nicholson, J. M. Fini, L. Meng, R. S. Windeler, E. M. Monberg, A. DeSantolo, K. Mukasa, V. Mikhailov, U. Feiste, W. Zhang, and R. Yu, "Transmission of commercial low latency interfaces over hollow-core fiber," *Journal of Lightwave Technology*, vol. 34, no. 2, pp. 314–320, 2016.

[147] Y. Hong, K. R. H. Bottrill, T. D. Bradley, H. Sakr, G. T. Jasion, K. Harrington, F. Poletti, P. Petropoulos, and D. J. Richardson, "Low-latency WDM intensity-modulation and direct-detection transmission over $>$100 km distances in a hollow core fiber," *Laser & Photonics Reviews*, vol. 15, no. 9, p. 2100102, 2021.

[148] M. R. Dizaji, C. J. Krückel, A. Fülöp, P. A. Andrekson, V. Torres-Company, and L. R. Chen, "Cross-phase-modulation-based wavelength conversion in low-stress silicon-rich nitride waveguide," in *2016 Optical Fiber Communications Conference and Exhibition (OFC)*, 2016, pp. 1–3.

[149] F. Gardes, V. Vitali, T. D. Bucio, H. Liu, J. M. L. González, F. Jurado-Romero, A. Ortega-Moñux, G. Churchill, J. C. Gates, J. Hillier, N. Kalfagiannis, D. Melati, I. Cristiani, J. H. Schmid, P. Cheben, J. G. Wangüemert-Pérez, Í. Molina-Fernández, C. Lacava, and P. Petropoulos, "Si-rich silicon nitride for nonlinear signal processing applications," in *Smart Photonic and Optoelectronic Integrated Circuits 2024*, S. He and L. Vivien, Eds., vol. 12890, International Society for Optics and Photonics. SPIE, 2024, p. 128900D.

Included papers A-D

Paper A

M. Raj, V. Ribeiro, G. Bouwmans, Y. Quiquempois, A. Mussot, P. Andrekson, M. Karlsson, “Investigation of Nonlinear Coupling and Parametric Interactions in Coupled Multi-Core Fibers”, *2025 European Conference on Optical Communications (ECOC)*, pp. 1–4, IEEE, 2025.

Paper B

M. Raj, T. Hayashi, P. Andrekson, M. Karlsson, “Statistical analysis of the temporal dynamics of coupling in strongly coupled multi-core fibers”, *Optics Express*, **34**, 25321–25333, 2026.

Paper C

M. Raj, L. A. Zischler, G. Di Sciullo, T. Hayashi, A. Mecozzi, C. Antonelli, M. Karlsson, "Statistical Characterization of Spatial and Polarization Mode Coupling in Field-Deployed Coupled-Core Multi-Core Fibers", *2026 European Conference on Optical Communications (ECOC)*, accepted for publication.

Paper D

L. A. Zischler, C. Lasagni, M. Raj, G. Di Sciullo, M. Karlsson, P. Serena, A. Bononi, T. Hayashi, A. Mecozzi, C. Antonelli, "Experimental Observation of Modal-Dispersion-Induced FWM Efficiency Increase and Nonlinearity Coefficient Characterization in Deployed Coupled-Core Multi-Core Fibers", *2026 European Conference on Optical Communications (ECOC)*, accepted for publication.